

The *JWST* EXCELS survey: The ages and abundances of $3 < z < 5$ massive quiescent galaxies show that downsizing was already in place by $z \simeq 4$

Ho-Hin Leung¹*, Adam C. Carnall¹, Elizabeth Taylor¹, Struan D. Stevenson¹, Aliza G. Beverage², Fergus Cullen¹, James S. Dunlop¹, Derek J. McLeod¹, Ross J. McLure¹, Ryan Begley³, Omar Almaini⁴, Stella Antonogiannaki¹, Karla Z. Arellano-Córdova¹, Laia Barrufet¹, Cecilia Bondestam¹, Callum T. Donnan⁵, Isaac J. B. Holst¹, Feng-Yuan F. Liu¹, Kate Rowlands^{6,7}, Ryan L. Sanders⁸, Dirk Scholte¹, Maya Skarbinski⁶, Thomas M. Stanton¹, and Vivienne Wild⁹

¹SUPA†, Institute for Astronomy, University of Edinburgh, Royal Observatory, Edinburgh EH9 3HJ, UK

²Department of Astronomy, University of California, Berkeley, CA 94720, USA

³Armagh Observatory and Planetarium, College Hill, Armagh, BT61 9DG, N. Ireland, UK

⁴School of Physics and Astronomy, University of Nottingham, University Park, Nottingham NG7 2RD, UK

⁵NSF’s National Optical-Infrared Astronomy Research Laboratory, 950 N. Cherry Ave., Tucson, AZ 85719, USA

⁶William H. Miller III Department of Physics and Astronomy, Johns Hopkins University, Baltimore, MD 21218, USA

⁷AURA for ESA, Space Telescope Science Institute, 3700 San Martin Drive, Baltimore, MD 21218, USA

⁸Department of Physics and Astronomy, University of Kentucky, 505 Rose Street, Lexington, KY 40506, USA

⁹SUPA, School of Physics & Astronomy, University of St Andrews, North Haugh, St Andrews, Fife KY16 9SS, UK

Accepted XXX. Received YYY; in original form ZZZ

ABSTRACT

We present deep, medium-resolution $\lambda = 1 - 5 \mu\text{m}$ *JWST*/NIRSpec spectroscopy for 14 quiescent galaxies at $3 < z < 5$ with $\log_{10}(M_*/\text{M}_\odot) > 10$, obtained as part of the EXCELS survey. We perform a complete re-reduction of these data, including a custom optimal-extraction approach to combat the spectral “wiggles” that result from undersampling of the NIRSpec spatial PSF. We constrain the star-formation histories and stellar metallicities of these objects via full-spectral fitting, finding a clear stellar age vs stellar mass correlation, in which more massive galaxies assembled their stellar mass at earlier times. This confirms spectroscopically that the archaeological “downsizing” trend was already in place by $z \simeq 4$. The slope of our measured relation ($\simeq 1.5$ Gyr per dex in stellar mass) is consistent with literature results at $0 < z < 3$. We do not observe objects with $\log_{10}(M_*/\text{M}_\odot) \lesssim 10.5$ and ages of more than a few hundred Myr at this epoch, suggesting that recently reported examples of higher-redshift quiescent galaxies at these masses are likely to soon rejuvenate. We measure relatively high stellar metallicities for the majority of our sample, consistent with similar objects at $0 < z < 3$. Finally, we explore evidence for α -enhancement in six older and more luminous galaxies within our sample, finding considerable disagreements in the chemical abundances measured using different stellar population models, different fitted rest-frame wavelength ranges, star-formation history models and fitting codes. We therefore conclude that inferring detailed stellar chemical abundances for the earliest quiescent galaxies remains challenging, and higher signal-to-noise spectra are required (SNR per resolution element > 100 for $R \simeq 1000$).

Key words: galaxies: evolution – galaxies: formation – galaxies: statistics – galaxies: stellar content – galaxies: high-redshift

1 INTRODUCTION

The most massive galaxies in the Universe provide a unique constraint on the process of galaxy formation, as they represent a limiting case for the underlying physics. In particular, extending the study of the most massive galaxies to progressively higher redshifts has repeatedly revolutionised our perspective on galaxy formation across the last several decades (e.g., Dunlop et al. 1996; Cimatti et al. 2004; Daddi et al. 2005).

As early as the mid-to-late 2000s, indications began to emerge of

galaxies at $z > 3$ that had already reached high stellar masses and subsequently shut down, or quenched, their star-formation activity (e.g., Caputi et al. 2004; Fontana et al. 2009). Improvements in the available datasets led to large and robust photometric samples beginning to emerge in the mid-to-late 2010s (e.g., Straatman et al. 2014, 2016; Merlin et al. 2018, 2019; Carnall et al. 2020), with spectroscopic confirmation following shortly thereafter (e.g., Glazebrook et al. 2017; Schreiber et al. 2018).

The advent of the *James Webb Space Telescope* (*JWST*) in 2022 quickly produced an explosion in the number of photometric candidate massive quiescent galaxies at $z > 3$ (e.g., Carnall et al. 2023a; Valentino et al. 2023), as well as in the quality and quantity of spec-

* E-mail: hleung2@roe.ac.uk

troscopic follow-up observations available (e.g., [Nanayakkara et al. 2024](#); [Glazebrook et al. 2024](#)), including the first spectroscopic confirmations significantly beyond $z = 4$ (e.g., [Carnall et al. 2023b](#); [Urbano Stawinski et al. 2024](#); [de Graaff et al. 2025](#)).

Extensive theoretical work has been undertaken to try to explain both the formation of so much stellar mass within such a short space of time (e.g., [Dekel et al. 2023, 2025](#); [Silk et al. 2024](#)), as well as the rapid quenching of star formation in the gas-rich high-redshift Universe (e.g., [Hartley et al. 2023](#); [Lagos et al. 2025](#); [Kimmig et al. 2025](#)). Significant interest has also developed into the fates of these extreme objects, for example whether they go on to form the cores of the most massive galaxies in the local Universe (e.g., [Baggen et al. 2023](#); [Beverage et al. 2024](#); [Rennehan 2024](#); [Remus & Kimmig 2025](#)).

However, such work has so far been guided only by very limited observational evidence. Robust, *JWST*-derived number densities for $z > 3$ massive quiescent galaxies have only been available from a handful of small area studies ($\lesssim 150$ sq. arcmin, e.g., [Carnall et al. 2023a](#); [Valentino et al. 2023](#); [Long et al. 2024](#); [Alberts et al. 2024](#); [Russell et al. 2025](#); [Baker et al. 2025a](#)), with the first larger-area studies only very recently becoming available ($\gtrsim 300$ sq. arcmin, e.g., [Baker et al. 2025b](#); [Stevenson et al. 2025](#); [Merlin et al. 2025](#)). More-detailed physical properties derived from spectroscopy are so far only available for individual bright and potentially unrepresentative objects (e.g., [Carnall et al. 2023b](#); [Setton et al. 2024](#); [Wu 2025](#); [de Graaff et al. 2025](#)).

Furthermore, much of the *JWST* spectroscopic data available so far at $z > 3$ is taken with the *JWST*/NIRSpec PRISM mode ($R = \lambda/\Delta\lambda \simeq 30 - 300$), far below the $R \simeq 1000$ required to robustly derive physical properties such as stellar ages and metallicities, using detailed study of individual spectral features (e.g., [Ocvirk et al. 2006](#); [Pacifici et al. 2012](#)). To probe in detail the mechanisms that result in the growth and quenching of early massive galaxies at $z > 3$, larger and more-representative galaxy samples with high signal-to-noise ratio (SNR) medium-resolution continuum spectroscopy are required.

A broad range of *JWST* medium-resolution high-SNR continuum spectroscopy already exists for massive ($\log_{10}(M_*/M_\odot) > 10$) quiescent galaxies at $z \simeq 1 - 3$, and is being widely exploited, demonstrating the value of such data (e.g., [Belli et al. 2024](#); [Kriek et al. 2024](#); [Park et al. 2024](#); [Davies et al. 2024](#); [Slob et al. 2024, 2025](#); [Beverage et al. 2025](#); [Bugiani et al. 2025](#); [Skarbinski et al. 2025](#)). Such works build upon ground-based efforts over many years to characterise the stellar populations in massive galaxies outside of the local Universe via deep optical-NIR continuum spectroscopy (e.g., [van der Wel et al. 2016](#); [McLure et al. 2018](#); [Pentericci et al. 2018](#); [Wild et al. 2020](#); [Beverage et al. 2024](#)).

One of the most fundamental results of this work is the archaeological downsizing trend. At fixed redshift, more-massive galaxies are found to have formed their stellar populations earlier in cosmic history than their less-massive counterparts (e.g., [Gallazzi et al. 2005, 2014](#); [Belli et al. 2019](#); [Carnall et al. 2019a](#); [Beverage et al. 2021](#); [Hamadouche et al. 2023](#); [Slob et al. 2024](#); [Merlin et al. 2025](#)). Downsizing is thought to arise primarily due to the baryon-to-star conversion efficiency in galaxy halos being a strong function of halo mass (e.g., [Moster et al. 2018](#)), with halos of masses $M_h \sim 10^{12} M_\odot$ being the most efficient. This means that the most massive halos at any given epoch typically passed through this highly efficient mass regime earlier than less-massive halos, forming the bulk of their stars during this time. There is also evidence that the peak conversion efficiency evolves modestly towards lower masses at later times, exacerbating this effect ([Behroozi et al. 2010](#)).

An alternative, more-empirical perspective on this is provided by [Abramson et al. \(2016\)](#), who argue that downsizing is a natural consequence of the redshift evolution of the star-formation main sequence (SFMS; e.g., [Speagle et al. 2014](#); [Popesso et al. 2023](#)). Higher star-formation rates (SFRs) at all stellar masses at earlier times and the less-than-unity slope of the SFMS ($d \log \text{SFR}/d \log M_* < 1$) mean that early-forming galaxies experienced rapid growth in stellar mass, quickly reaching relatively low star-formation efficiencies (i.e., quenching) at the high-mass end of the SFMS. For galaxies that formed later, lower SFRs at all stellar masses lead to slower mass assembly and thus more-extended star-formation histories (SFHs).

Dry mergers after quenching have also been suggested as a contributing factor to downsizing ([Cattaneo et al. 2008](#)). Galaxies that assembled and quenched earlier are often central galaxies in groups and clusters, and so have many opportunities to further grow in mass via dry mergers. Other ideas centred on quenching mechanisms that could become less effective at high-redshift have also been proposed to contribute to downsizing, such as active galactic nucleus (AGN) feedback (e.g., [Scannapieco et al. 2005](#); [Croton et al. 2006](#)), virial-shock heating (e.g., [Dekel & Birnboim 2006](#); [Rodríguez-Puebla et al. 2017](#)) and environmental effects (e.g., [Taylor et al. 2023](#)).

Further key insights into the formation and quenching of massive quiescent galaxies can be gained by the study of their stellar metallicities. Foundational work in the local Universe established the existence of a stellar metallicity vs stellar mass relationship (e.g., [Gallazzi et al. 2005](#); [Panter et al. 2008](#)), which flattens at the highest masses. The fact that local star-forming galaxies display lower stellar metallicities than their quiescent counterparts at fixed stellar mass has been interpreted as suggesting that an extended process of gas exhaustion over several billion years is the primary mechanism that quenched low-redshift quiescent galaxies (e.g., [Peng et al. 2015](#); [Trussler et al. 2020](#)). However the many free parameters and degeneracies involved in even the simplest one-zone analytic chemical evolution models make the interpretation of such results extremely challenging. For example, recent results from [Leung et al. \(2024\)](#) demonstrate that an increase in stellar metallicity can also occur as a result of an intense, short-timescale starburst event immediately prior to quenching.

More recently, the analysis of quiescent galaxy stellar metallicities has been extended to higher redshift (e.g., [Gallazzi et al. 2014](#); [Kriek et al. 2016, 2019](#); [Carnall et al. 2019a, 2022](#); [Jafariyazani et al. 2020](#); [Beverage et al. 2024](#); [Cheng et al. 2024](#)). The long timescales of many billions of years involved in gas exhaustion models immediately suggests an alternative quenching mechanism must dominate at the cosmic noon epoch and beyond ($z \gtrsim 1$), with many studies focusing on the possibility of rapid quenching via gas expulsion driven by strong AGN feedback (e.g., [Beverage et al. 2021](#)). Evidence for mild evolution in the quiescent stellar mass vs stellar metallicity relation towards higher redshifts is mixed, however strong evolution is now effectively ruled out, at least as far as $z \simeq 3$ ([Lonoce et al. 2015](#); [Onodera et al. 2015](#); [Estrada-Carpenter et al. 2019](#); [Beverage et al. 2025](#)).

Extending this substantial body of work beyond $z = 3$ is the primary motivation for the *JWST* Cycle 2 Early eXtragalactic Continuum and Emission-Line Science (EXCELS) Survey ([Carnall et al. 2024](#), Programme ID: 3545, PI: Carnall; Co-PI: Cullen). EXCELS targeted a representative sample of 14 candidate massive quiescent galaxies at $3 < z < 5$ in the PRIMER UDS field, obtaining ultra-deep, medium-resolution continuum spectroscopy from $\lambda = 1 - 5 \mu\text{m}$ for all these objects. In this work, we present this representative spectroscopic sample and perform full spectrophotometric fitting, in combination with the available photometry, to derive detailed physical

properties for these objects. In particular, we focus on their stellar ages and metallicities. In companion papers, we investigate the processes giving rise to line emission in these objects (Stevenson et al. 2025), as well as evidence for neutral outflowing gas via absorption line analysis (Taylor et al. 2026).

This paper is structured as follows. In Section 2 we introduce our photometric and spectroscopic data and reduction methodology. We also present our fiducial full-spectral-fitting methodology using the BAGPIPES code and Bruzual & Charlot (2003) stellar population models, by which our main results are derived. These results are presented in Section 3. In Section 4 we investigate alternative full-spectral-fitting approaches using stellar population model libraries that allow for enhanced α -element abundances, instead of the standard approach of assuming scaled-solar abundances for all elements. We present our conclusions in Section 5.

All magnitudes are quoted in the AB system (Oke & Gunn 1983). For cosmological calculations, we adopt $\Omega_m = 0.3$, $\Omega_\Lambda = 0.7$, and $H_0 = 70 \text{ km s}^{-1} \text{ Mpc}^{-1}$. We assume a Kroupa (2001) stellar initial mass function (IMF), and take solar metallicity $Z_\odot = 0.0142$ (Asplund et al. 2009). We re-scale all metallicity measurements quoted from the literature to this solar metallicity value for direct comparison. We average SFRs over a 100 Myr period throughout.

2 DATA REDUCTION AND FITTING METHODOLOGY

2.1 PRIMER photometric data

The primary photometric dataset supporting this work is the large public *JWST* Cycle 1 programme Public Release IMaging for Extragalactic Research (PRIMER; Dunlop et al. in prep.; Dunlop et al. 2021), which provides contiguous 8-band NIRCam imaging (F090W, F115W, F150W, F200W, F277W, F356W, F410M and F444W) plus 2-band MIRI imaging (F770W and F1800W) in the UDS and COSMOS fields.

The photometric data used in this work comes from the PRIMER UDS catalogue described in Begley et al. (2025). This is an updated version of the photometric catalogue used to select the EXCELS sample, as described in Carnall et al. (2024). In this section we present a brief overview of the Begley et al. (2025) photometric catalogue.

Begley et al. (2025) reduce the available NIRCam data using the PENCIL software (PRIMER Enhanced NIRCam Image-processing Library; Magee et al. in prep.), which builds on the standard *JWST* data reduction pipeline (v1.10.8; pmap>1118). PENCIL includes custom additional routines for background subtraction, 1/f noise correction and snowball/wisp removal.

The resulting NIRCam mosaics are then PSF-homogenised to the F444W band using kernels constructed by stacking bright, unsaturated stars in the PRIMER field. The PRIMER data is also supplemented with deep optical *HST*/ACS F435W, F606W and F814W imaging (Grogan et al. 2011; Koekemoer et al. 2011). The EXCELS sample was selected only within the area that has coverage in all three *HST* bands, meaning we have full $\lambda = 0.4 - 5 \mu\text{m}$ coverage for all our objects. We use the *HST* mosaics produced as part of the Hubble Legacy Field project (Illingworth et al. 2016; Whitaker et al. 2019). These *HST* data are also similarly PSF-homogenised to the PRIMER F444W-band imaging.

The multi-wavelength catalogue is then constructed using Source Extractor (Bertin & Arnouts 1996) in dual image mode, with the unconvolved F356W mosaic used as the detection band in all cases. Fluxes are extracted in $0.5''$ -diameter apertures, and these aperture

fluxes are corrected to total using the FLUX_AUTO output from Source Extractor (Kron 1980). We then apply a further 10 per cent correction following McLeod et al. (2024) to account for flux not included within the Kron aperture.

The 14 EXCELS quiescent galaxies at $z > 3$ selected by Carnall et al. (2024) are all recovered from this new catalogue via a close positional match. Their celestial coordinates and spectroscopic redshift are listed in Table 1 of Carnall et al. (2024). All 14 objects have coverage in all 11 *HST*+NIRCam photometric bands described above. Additionally, as demonstrated in Stevenson et al. (2025), all 14 are still selected from the new Begley et al. (2025) catalogue as $z > 3$ massive quiescent galaxy candidates via a similar process to that employed by Carnall et al. (2024).

Stevenson et al. (2025) also consider mass-completeness limits for their sample of photometrically selected $z > 3$ massive quiescent galaxy candidates (see their fig. 1), concluding that their F356W < 26 sample is more than 99 per cent mass complete at $\log_{10}(M_*/M_\odot) > 10$. The EXCELS sample is selected requiring F356W < 25, meaning that it is mass complete at $\log_{10}(M_*/M_\odot) > 10.4$. As discussed in Section 3, the stellar masses we derive for all 12 of the 14 EXCELS objects for which we are able to obtain robust spectral fits are above this threshold.

2.2 EXCELS spectroscopic data

The EXCELS dataset is described in full in Carnall et al. (2024); here we provide a brief summary. The survey consists of 4 NIRSpec pointings within the PRIMER UDS imaging area, which were each observed with all 3 medium-resolution gratings using different mask configurations in order to maximise the number of objects for which rest-frame optical coverage could be obtained. The exposure times obtained were $\simeq 4$ hours in G140M, $\simeq 5.5$ hours in G235M and $\simeq 4$ hours in G395M. As the top-priority targets for the survey, the 14 objects that are the focus of this work were observed in all three gratings, providing continuous wavelength coverage from $1 - 5 \mu\text{m}$ (excepting objects with traces that cross the NIRSpec detector gap, which have short interruptions in coverage).

2.2.1 Initial spectroscopic reduction with the NIRSpec pipeline

We perform a new, customised reduction of the 14 EXCELS spectra for massive quiescent galaxies at $z > 3$ using a modified version of the standard *JWST* reduction pipeline¹ (Bushouse et al. 2025, version 1.19.1). We use the CRDS_CTX = jwst_1413.pmap version of the *JWST* Calibration Reference Data System (CRDS) files.

First, we obtain the level 1 “uncal” products from the Mikulski Archive for Space Telescopes (MAST). These products are processed by the level 1 pipeline (calwebb_detector1) using default configurations except we turn on the clean_flicker_noise step to remove the effects of 1/f noise from the exposures. For this reduction step, we set fit_method to median, mask_science_region to True, background_method to None and n_sigma to 2. These choices were arrived at after extensive experimentation to determine which configuration produces the cleanest results in unilluminated areas of the detector.

We next run the resulting level 2a “rate” products through the level 2 pipeline (calwebb_spec2) using the default configuration options. Background subtraction is performed on each of the three nod positions by subtracting the sigma-clipped average of the other

¹ <https://github.com/spacetelescope/jwst>

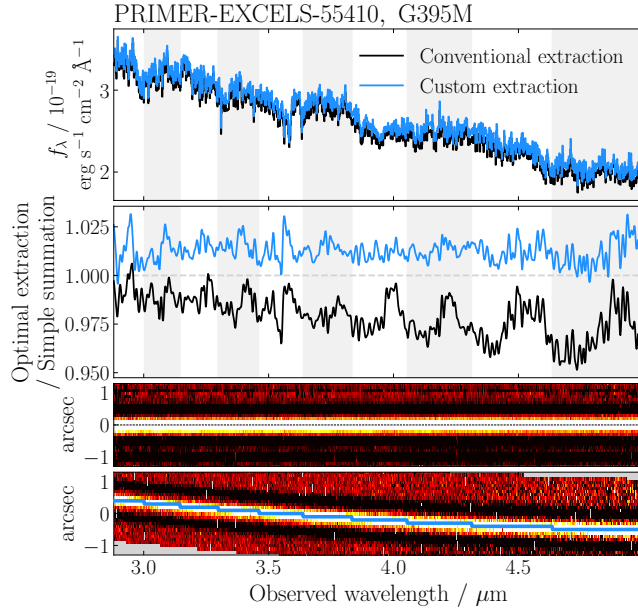


Figure 1. A comparison of different optimal extraction methods applied to our NIRSpec data (see Section 2.2.2). Our custom wavelength-varying 1D optimal extraction is shown in blue; the more-conventional fixed-kernel method is shown in black. The top panel shows the 1D extracted spectrum from the G395M grating for PRIMER-EXCELS-55410 (ZF-UDS-7329), extracted using the two methods. The second panel shows the ratio between the extracted spectrum and the spectrum obtained from simply summing the central 5 rows of the 2D spectrum (roughly the projected size of one shutter). The third panel shows the level 3 pipeline output 2D spectrum (after `drizzle` resampling), and the bottom panel shows the level 2 2D spectrum for one of the three nod positions (before `drizzle` resampling). The pixel containing the object centroid is marked with a blue line in the bottom panel. In the top two panels we also colour with alternating grey and white bands wavelength ranges for which the centroid of the trace falls on the same pixel row in the bottom panel. Periodic fluctuations at a ≈ 5 per cent level can be seen in the black spectrum, with the pattern repeating every time the centroid shifts to the next pixel down in the bottom panel. Our custom optimal extraction method mitigates these fluctuations by using a wavelength-varying extraction kernel.

two nod positions (using the default 3 sigma threshold). For all observations of PRIMER-EXCELS-52467 and for two nods in the G140M grating observations of PRIMER-EXCELS-112990 only one background nod was used, in order to avoid contamination in the other background shutter.

We then mask any pixels in the resulting level 2b “cal” files flagged with any among a customised list of data quality bit-masks². We also perform additional manual masking of bad pixels, snowballs not caught by the automatic detection step in the level 1 pipeline, bleeding from hot pixels, and contamination from overlapping open shutters or bright stars. Following this, we pass all “cal” products into the level 3 pipeline (`calwebb_spec3`) using the default configuration options.

² Bits: 0, 1, 3, 4, 6, 7, 10, 11, 12, 13, 16, 17, 18, 19, 20, 21, 24, 26, 27, 29 and 30 (see https://jwst-pipeline.readthedocs.io/en/latest/jwst/references_general/references_general.html#data-quality-flags)

2.2.2 Optimal 1D spectral extraction

We extract 1D spectra from the level 3 output “s2d” files via optimal extraction (Horne 1986). When initially performing optimal extraction using the same fixed kernel at all wavelengths (constructed via Gaussian fits to the wavelength-collapsed 2D spectra), we noticed ≈ 5 per cent systematic fluctuations (“wiggles”) in the continua of the extracted spectra (e.g., Perna et al. 2023; Dumont et al. 2025). This effect is demonstrated in Fig. 1, where our initial fixed-kernel optimal extraction run is compared with a simple sum over the central 5 rows of the rectified 2D spectrum (“s2d” output) for an example object. The top panel shows the fixed-kernel extraction in black, and the ratio of the fixed-kernel extraction to the simple sum extraction is shown in black in the middle panel. The optimal extraction is expected to produce a very similar spectrum to the simple sum, with higher SNR, however periodic wiggles are clearly visible.

The bottom panels of Fig. 1 show the rectified “s2d” (above) and unrectified “cal” (below) 2D spectra for this object. The former is a stack of all three nod positions, the latter is for a single example nod position. It can be seen that the wiggles in the black line in the middle panel have periods in wavelength that exactly match the pattern of the object’s centroid shifting from one row to the next in the unrectified (bottom) 2D frame, shown by the blue horizontal line.

This pattern arises due to the `resample_spec` step in the level 3 pipeline, which uses the `drizzle` algorithm to resample the “cal” products from the three nod positions into a single rectified product (Fruchter & Hook 2002). The algorithm by default assumes that flux is uniformly distributed within each pixel, since the true distribution of flux at higher spatial resolution is not known. The pixel scale for NIRSpec is $0.1''$, meaning the spatial point spread function is significantly undersampled, and so the assumption of uniformly distributed flux within pixels is not valid for compact sources such as ours. This leads to different results depending on where the object centroid falls relative to the spatial pixels. For example, the object trace is wider in the spatial direction when the centroid falls on the boundary between two pixels, and narrower when the centroid falls in the centre of a pixel. This means that our assumption of a single fixed-width kernel at all wavelengths is a poor representation of the data, leading to the ≈ 5 per cent systematic fluctuations seen in Fig. 1.

We therefore instead perform a custom wavelength-varying 1D optimal extraction of our 2D spectra. We begin by fitting a Gaussian to the wavelength-collapsed 2D spectrum, as previously, to provide an initial estimate of the centroid position and σ width. Next, we isolate only the rows in the 2D spectra that are within $\pm 3\sigma$ of the fitted centroid. We then loop over all wavelength bins, summing in the wavelength direction within a boxcar of ± 25 pixels ($\approx 300, 500$ and 900 \AA for G140M, G235M and G395M, respectively). Within each iteration, we then calculate the total SNR of the wavelength-collapsed spectrum slice. If $\text{SNR} \geq 5$, we flux normalise the wavelength-collapsed spectrum slice and use this directly as the optimal extraction weights in this wavelength bin. If $\text{SNR} < 5$, we instead use the initial Gaussian fit over all wavelengths for our optimal extraction weights at this wavelength.

An example result from this custom extraction method is shown in blue in Fig. 1, and is compared against the conventional method described above, which is shown in black. It can be seen that the fluctuations in sync with the shifting of the trace’s centroid have been removed. Thus, the amplitude of the systematic fluctuations with respect to the simple sum over 5 pixel rows has been reduced to ≈ 1 per cent.

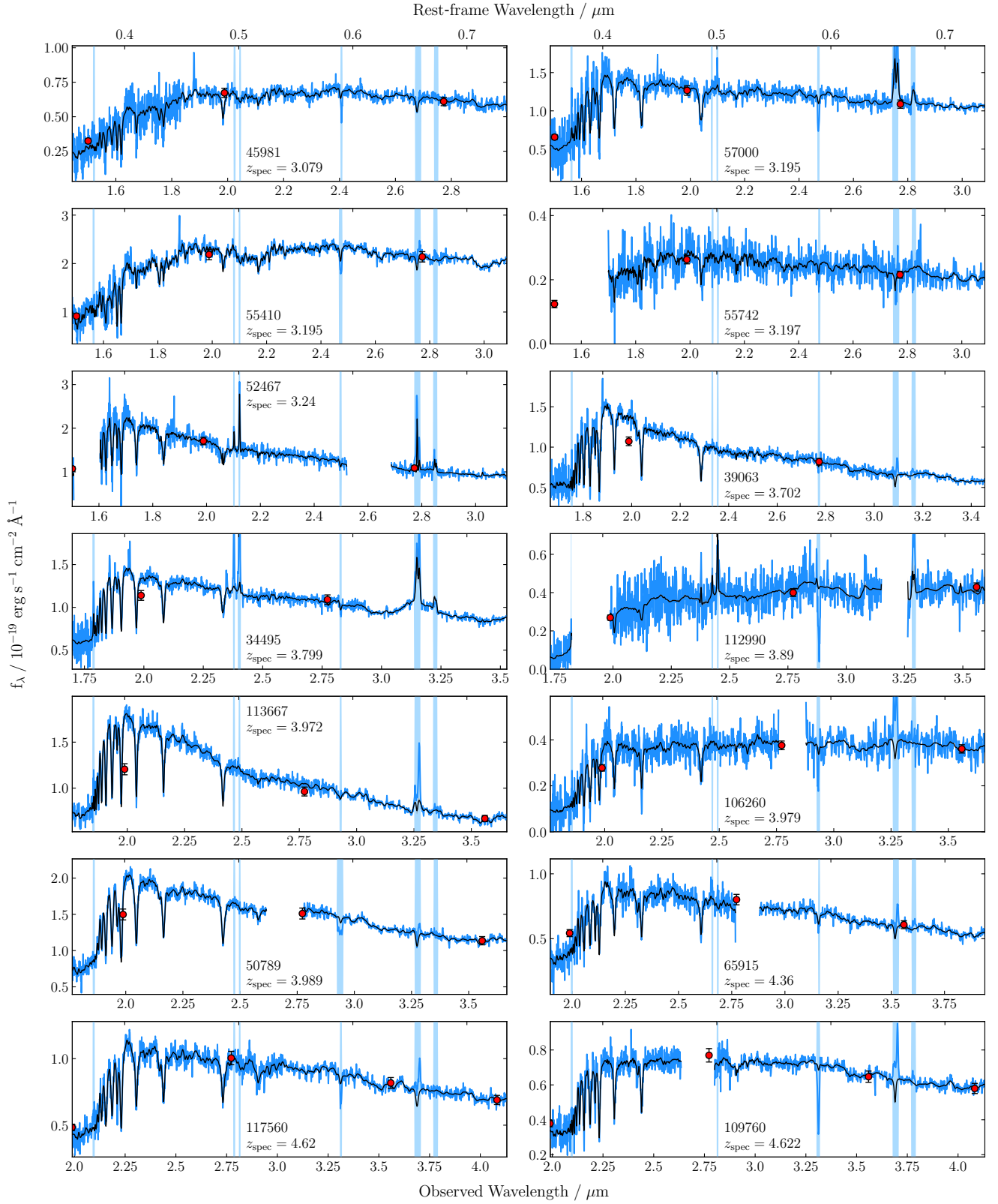


Figure 2. The spectral energy distributions (SEDs) and spectra for the 14 massive $z > 3$ quiescent galaxies observed as part of EXCELS. The calibrated EXCELS NIRSpec observations within the rest-frame wavelength range $3540 - 7350 \text{ \AA}$ used in our primary fitting methodology are shown in blue. PRIMER NIRCam photometry within this wavelength range are shown as red dots. The posterior median model spectra fitted using BAGPIPES are shown in black. Vertical blue bars mark the regions masked during fitting.

Table 1. Model priors used when performing Bayesian fits of the EXCELS spectra jointly with *HST+JWST* photometry (see Section 2.3 for a full description). Some parameters have prior shape \log_{10} uniform, which indicates a flat prior in logarithmic space $\log(X) \sim U(\log(\min), \log(\max))$. Note that σ_{disp} is not the intrinsic velocity dispersion of the galaxy, as it does not account for the finite resolution of the spectral templates or observational data.

Type	Parameter	Form	Min	Max
SFH	$\log_{10}(M_*/M_\odot)$	Uniform	0	13
	Stellar metallicity Z_*/Z_\odot	Uniform	0.007	3.52 [†]
	Double-power-law falling slope α	\log_{10} Uniform	0.1	1000
	Double-power-law rising slope β	\log_{10} Uniform	0.1	1000
	Double-power-law turnover time τ / Gyr	Uniform	0.1	t_{obs}
Dust	A_V / mag	Uniform	0	4
	Deviation from Calzetti slope δ	Gaussian ($\mu = 0, \sigma = 0.1$)	-0.3	0.3
	Strength of 2175Å bump B	Uniform	0	5
	Birth cloud factor η	Fixed = 2	-	-
AGN*	Continuum flux at 5100Å f_{5100} / $\text{erg s}^{-1} \text{cm}^{-2} \text{\AA}^{-1}$	Uniform	0	10^{-19}
	Spectral index at $\lambda_{\text{rest}} < 5100\text{\AA}$ $\alpha_{\lambda, < 5000}$	Gaussian ($\mu = -1.5, \sigma = 0.5$)	-2	2
	Spectral index at $\lambda_{\text{rest}} > 5100\text{\AA}$ $\alpha_{\lambda, > 5000}$	Gaussian ($\mu = 0.5, \sigma = 0.5$)	-2	2
	Broad H α normalisation $f_{\text{H}\alpha, \text{broad}}$ / $\text{erg s}^{-1} \text{cm}^{-2}$	Uniform	0	2.5×10^{-17}
	Broad line velocity dispersion σ_{AGN} / km/s	\log_{10} Uniform	1000	7000
GP noise	Uncorrelated amplitude (white noise scaling) s	\log_{10} Uniform	0.1	10
	Correlated amplitude σ	\log_{10} Uniform	10^{-4}	10^{-1}
	Period/length scale ρ	\log_{10} Uniform	0.04	4.0
	Dampening quality factor Q	Fixed = 0.49	-	-
Miscellaneous	Redshift	Gaussian ($\mu = z_{\text{spec}}, \sigma = 0.01$)	$z_{\text{spec}} - 0.05$	$z_{\text{spec}} + 0.05$
	Stellar velocity dispersion σ_{disp} / km/s	\log_{10} Uniform	50	500

[†] Prior limits for stellar metallicity are 0.005–2.5 Z_\odot for $Z_\odot = 0.02$ as assumed in the [Bruzual & Charlot \(2003\)](#) stellar population models. For our solar metallicity value at $Z_\odot = 0.0142$, this converts to 0.007–3.52 Z_\odot .

* Component not included when fitting galaxies 45981, 50789, 55410, 55742, 65915 and 117560.

2.2.3 Combination of separate gratings and correcting slit loss

To combine 1D spectra from the three separate gratings for each object, we first calculate the mean flux in the overlapping wavelength regions, then scale the G140M and G395M spectra to the normalisation of the G235M data. In the absence of any detector gaps in the overlapping regions, we degrade the resolution of the higher-resolution (shorter-wavelength) grating in both overlapping regions to match the lower-resolution grating using SPECTRES ([Carnall 2017](#)). If a detector gap is present in one of the gratings within the overlapping region, we instead resample the grating with the gap to match the resolution of the grating without the gap. Lastly, all overlapping regions are combined through taking a simple mean of the pixel values from the two gratings. Due to their very noisy G140M spectra, we only combine the G235M and G395M spectra for three galaxies (55742, 106260 and 112990).

To account for slit losses and potentially imperfect spectrophotometric calibration, we then scale the joined spectrum for each object to match the best fit model from an initial fit to only the *HST+JWST* photometry described in Section 2.1. The fit is performed using the Bayesian spectral fitting code BAGPIPES ([Carnall et al. 2018, 2019a](#)), with an almost identical model configuration and priors to those described in Section 2.3, except we remove the spectroscopy-specific Gaussian process and velocity dispersion components, and do not include AGN contributions to limit complexity. We also fix the redshifts to the values measured manually by the EXCELS team, as described in [Carnall et al. \(2024\)](#).

To scale our joined spectra to these best-fit models, we first create a temporary degraded EXCELS spectrum from the joined gratings by binning in groups of 5 pixels. The best-fit model spectrum is then resampled onto the same coarse wavelength grid using SPECTRES. We

next calculate the ratio between the resampled model spectrum and a rolling median of the degraded EXCELS spectrum, calculated using a window that spans 101 bins ($\sim 3000 - 9000 \text{\AA}$). These smoothing steps are performed to prevent the recalibration from altering the spectral shape on short wavelength scales, which risks altering individual emission/absorption line equivalent widths or spectral break strengths.

Finally, we fit a 15th order Chebyshev polynomial to these calculated ratios as a function of wavelength (e.g., [Cappellari 2017](#)), and recalibrate our joined EXCELS spectra according to this polynomial. Our final joined and calibrated spectra for the 14 EXCELS quiescent galaxies at $3 < z < 5$ are shown in Fig. 2.

2.3 Bayesian spectrophotometric fitting

To measure galaxy properties, we then perform Bayesian full spectral fitting of the spectra for our 14 EXCELS massive quiescent galaxies at $3 < z < 5$, reduced and calibrated as described in Section 2.2, in combination with the *HST+JWST* photometry described in Section 2.1. Fitting is performed using BAGPIPES (version 1.3.1), with a similar model configuration and priors to those adopted in [Carnall et al. \(2024\)](#). In Table 1, we list all fitted model parameters and their priors. All input spectra are first truncated to rest-frame wavelengths from $3540 - 7350 \text{\AA}$ before being passed into BAGPIPES, which is the wavelength range spanned by the empirical and high-spectral-resolution MILES library in the [Bruzual & Charlot \(2003\)](#) models. We additionally mask the [O II], [O III], [N II], [S II] and H α emission lines (but not H β), as well as the Na D absorption line, due to potential non-stellar contributions.

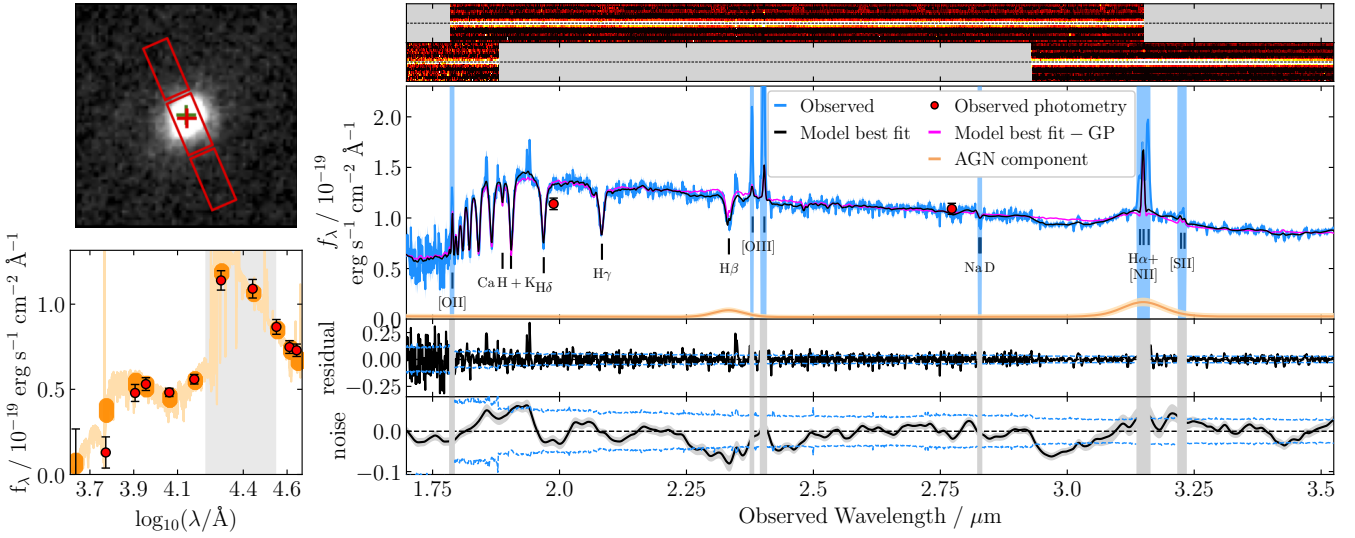


Figure 3. Detailed BAGPIPES full-spectral fitting of PRIMER-EXCELS-34495, shown as an example of the process described in Section 2.3. **Top left:** A PRIMER F277W cutout image of the galaxy. The overlaid rectangles mark the MSA slit positions for the first of the three G235M nod positions, while the cross marks the extraction centroid (see Section 2.2.2) **Top right:** Observed 2D spectra for the three medium resolution gratings. **Central right:** Our 1D spectroscopic extraction within the rest-frame wavelength range 3540–7350 Å (blue) and *HST*+*JWST* observed photometry (red points). Plotted on top are the fitted posterior median model spectrum (black line), the physical model spectrum (magenta line: posterior median model with the posterior median GP component subtracted) and the fitted AGN component (orange line). **Lower right:** Residuals (black) between our fitted model and data, along with the input observational uncertainties (dotted blue lines) scaled by our s parameter. **Bottom right:** The fitted additive GP noise component in black, along with the same scaled input observational uncertainties. The y-axes of both the residual and noise panels have the same units as the central panel, but an expanded scale. In the central, residual and noise panels, the vertical shaded bars mark the regions masked during fitting. **Bottom left:** The full observed multi-band photometry (red points), described in Section 2.1, and the corresponding model posteriors (orange patches). The orange curve shows the posterior median model spectrum and the shaded region marks the rest-frame wavelength range from 3540–7350 Å.

2.3.1 Bagpipes full spectral fitting approach

Within BAGPIPES, we employ the [Bruzual & Charlot \(2003\)](#) stellar population synthesis models (2016 version, described in [Chevallard & Charlot 2016](#)), which incorporates the high-resolution rest-frame optical empirical stellar spectral templates from the MILES library ([Sánchez-Blázquez et al. 2006](#); [Falcón-Barroso et al. 2011](#)). We assume the initial mass function of [Kroupa \(2001\)](#), and a double-power-law SFH model (e.g., [Carnall et al. 2019b](#)). We assume a uniform and time-invariant stellar metallicity for each galaxy, which is allowed to vary with a uniform prior.

We model nebular emission using the CLOUDY photoionization code ([Ferland et al. 2017](#)), with an approach based on that of [Byler et al. \(2017\)](#). The nebular metallicity is fixed to the stellar value, and the ionization parameter is held fixed at $\log_{10}(U) = -3$.

We model dust attenuation using the variable-slope model from [Salim et al. \(2018\)](#), which is based on a power-law perturbation of the [Calzetti et al. \(2000\)](#) dust law. Any stars younger than 10 Myr are assumed to be more attenuated than older stars by a factor $\eta = 2$, as they are assumed to still be surrounded by their birth clouds. We model intergalactic medium attenuation using the [Inoue et al. \(2014\)](#) model. We model velocity dispersion within our target objects using a Gaussian broadening in velocity space with width σ_{disp} , which is varied with a logarithmic prior.

According to the galaxies' location on the BPT and WHAN diagrams ([Baldwin et al. 1981](#); [Cid Fernandes et al. 2011](#)), 6/14 of our sample could have contributions from an AGN in their spectra ([Stevenson et al. 2025](#)). Therefore, following [Carnall et al. \(2023b\)](#), we also test the inclusion of an AGN component, consisting of AGN continuum emission, as well as broad H α and H β emission lines. The

continuum model follows the broken power law from [Vanden Berk et al. \(2001\)](#), which is described by a break at $\lambda_{\text{rest}} = 5000\text{\AA}$ and two power-law indices ($\alpha_{\lambda, < 5000}$ and $\alpha_{\lambda, > 5000}$). The normalisation of the continuum is parametrized via its flux at rest-frame 5100Å (f_{5100}). The broad H α component is modelled with a Gaussian profile, where we fit its normalisation ($f_{\text{H}\alpha, \text{broad}}$) and velocity dispersion (σ_{AGN}). We use the same parameters to model the broad H β emission line, but divide its normalisation by 2.86 assuming case B recombination.

Although we fit all 14 galaxies using the model including the AGN component, when compared to results from fitting without the AGN component, we see minimal changes in estimated properties (e.g., $\Delta \log_{10}(M_*/M_\odot) < 0.02$; $\Delta \text{Age} < 0.03$ Gyr). Thus, for the 6 galaxies that lie outside any AGN regions in the WHAN diagram at $> 1\sigma$ confidence (45981, 50789, 55410, 55742, 65915 and 117560; see fig. 13 in [Stevenson et al. 2025](#)), we report results from their fits without the AGN model. For the other 8 objects we report results for the run including the AGN model, however we only observe a significant AGN contribution in 34495, which exhibits a clearly visible broad H α component. Spectrum decomposition following [Krishna et al. \(2025\)](#) also showed a significant AGN contribution in 34495 alone. We therefore conclude that contamination of the continuum emission from our other galaxies by AGN is very weak, if any. Therefore, we consider our results robust against AGN contamination.

Since spectrophotometric calibration has already been performed on the input spectra in Section 2.2, we do not use the multiplicative Chebyshev calibration polynomial that was employed in [Carnall et al. \(2024\)](#). Instead, we include an additive Gaussian Process (GP) correlated noise model. This allows for the correction of any remaining minor calibration imperfections, as well as model-data mismatch,

and also properly accounts for correlated noise across wavelength bins in the observed spectra (Carnall et al. 2019a). The GP model uses a stochastically driven damped simple harmonic oscillator kernel, as introduced in Leung et al. (2024) and Leung et al. (2025), implemented through the `celerite2` python package (Foreman-Mackey et al. 2017; Foreman-Mackey 2018). To model potentially underestimated observational uncertainties in our input spectra (e.g., Maseda et al. 2023), we also include a multiplicative factor (s) on the spectroscopic uncertainties, which is varied with a logarithmic prior. Sampling of the model posterior within BAGPIPES is performed using the NAUTILUS nested sampling algorithm (Lange 2023a).

The posterior median models fitted to our spectroscopic data by this process are shown with black lines in Fig. 2. We also show one fit in more detail for object PRIMER-EXCELS-34495 in Fig. 3. The top left panel shows the position of the open NIRSpec MSA shutters of the EXCELS G235M observations overlaid on a PRIMER F277W cutout image of the galaxy. The top right panel shows the 2D spectra for the 3 individual gratings observed as part of EXCELS. The central panel shows our 1D spectroscopic extraction (blue), with observed photometry (red points). Over-plotted are the fitted posterior median model spectrum (black), the physical model spectrum (fitted spectrum – GP component, magenta) and the best fit AGN component (red). In the lower panels we also show the residual spectrum and the GP noise model. The bottom left panel shows the full *JWST+HST* multi-band photometric data for this galaxy, and the full best fit model spectrum.

2.3.2 Consistency checks on our full-spectral-fitting methodology

To test the dependence of our results on our assumed SFH parameterisation, we also repeated our fits using the non-parametric ‘‘continuity’’ SFH model (Leja et al. 2019), following the binning implementation of Park et al. (2024). We find no significant change in the measured SFHs and subsequent results when switching our fiducial double-power-law model for the continuity non-parametric model (estimates of t_{50} , stellar mass and metallicity are within 1σ of the fiducial estimates, as was also found in Carnall et al. 2023b). Thus, we conclude that our findings are not strongly dependent on the SFH model assumed.

The GP model corrections on our best-fit spectral models typically have a magnitude < 4 per cent of the input spectrum, and are hence typically smaller than the observational uncertainties (see the bottom right panel in Fig. 3). To investigate the impact of our GP model, we repeated our fits, firstly with a 38th order multiplicative Chebyshev polynomial instead of the GP noise model, then again with both the polynomial and GP models. These tests produce estimated SFHs and galaxy bulk properties (e.g., stellar mass, mass-weighted age) within the 1σ uncertainty region of our fiducial model. Therefore, we conclude that our choice of the GP model over the polynomial method does not significantly impact our results.

3 RESULTS

The properties of the 14 EXCELS $z > 3$ massive quiescent galaxies measured via the full-spectral-fitting approach laid out in Section 2.3 are summarised in Table 2. Their celestial coordinates can be found in Table 1 of Carnall et al. (2024). Two galaxies with the noisiest EXCELS spectra and poor coverage of the Balmer lines (55742 and 112990; SNR per $\text{\AA} < 3$ averaged over $5100 < \lambda_{\text{rest}} < 6400 \text{\AA}$) returned fitted parameters and SFHs with very large uncertainties, and we therefore exclude these galaxies from all further analysis. Our

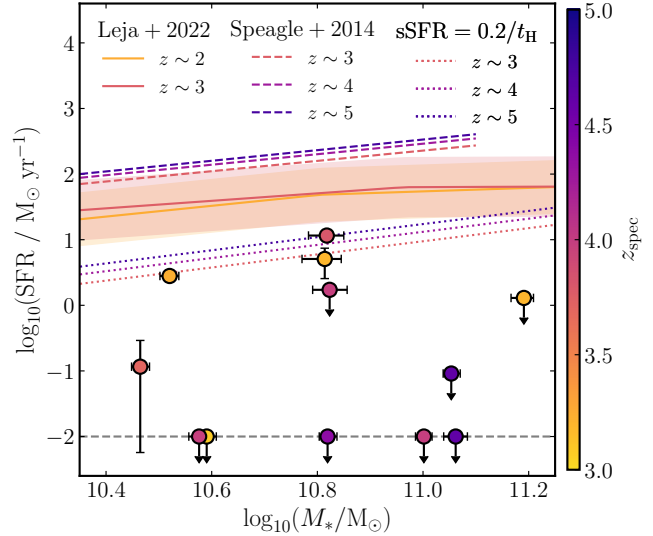


Figure 4. The stellar masses of our sample of 12 massive quiescent galaxies plotted against their SFRs (averaged over 100 Myr), with both quantities measured from full spectral fitting. For data points with posterior median $\log_{10}(\text{SFR}/\text{M}_\odot \text{ yr}^{-1}) < -2$, we show 3σ upper limits. We also set a minimum SFR upper limit at $\log_{10}(\text{SFR}/\text{M}_\odot \text{ yr}^{-1}) < -2$ (grey dashed lines) to limit the vertical dynamic range of the figure. The symbols are coloured according to their observed redshifts. We show the SFMS from Leja et al. (2022) at $z \sim 2$ and $z \sim 3$ with solid lines and shaded regions. We show the SFMS from Speagle et al. (2014) at $z \sim 3$, $z \sim 4$ and $z \sim 5$ with dashed lines. We also mark the threshold $\text{sSFR} = 0.2/t_H$ at $z \sim 3$, $z \sim 4$ and $z \sim 5$ with dotted lines. All galaxies in our sample have SFRs at least 0.5 dex below the SFMS at the corresponding redshift, and are below the sSFR threshold in all but one case. The final object, 34495, falls $\approx 2\sigma$ above this limit.

results are summarised in Figs 4 and 5, and compared with results from the literature in Fig. 6. We show a gallery of our fitted SFH posteriors in Fig. A1.

3.1 Current star-formation rates

For 9/12 of the galaxies with spectroscopic data of a high enough quality to obtain robust results we recover $\text{SFR} < 1 \text{ M}_\odot \text{ yr}^{-1}$ at the time of observation. Although the other three (34495, 52467 and 57000) appear not to have fully shut down star formation when observed, as shown in Fig. 4, all but one of our objects (34495) falls below the $\text{sSFR} < 0.2/t_H$ threshold used by Carnall et al. (2024) to select the EXCELS sample. The final object, 34495, is within 2σ of this threshold. Our SFR estimates are all > 0.5 dex below the star-formation main sequence (SFMS) at $z \sim 3$, as reported by both Speagle et al. (2014) and Leja et al. (2022). Given this, as well as their sharply declining SFHs before observation, we consider all our objects to be quenched.

From the final 2 objects for which we do not obtain robust results via our full-spectral-fitting methodology, 112990 shows some signs of a higher star-formation rate, consistent with the spectrum showing detectable [O III] line emission in Fig. 2. However, the poor quality of the spectrum makes it challenging to constrain the SFR precisely (SNR per $\text{\AA} = 2.74$ and missing the Balmer break region). A contamination rate of 1 – 2 objects from our sample of 14 is consistent with the 8 ± 3 per cent spectroscopic contamination rate derived by Stevenson et al. (2025) for a larger photometric sample selected via the same process.

Table 2. Galaxy physical properties derived for our EXCELS sample from the full spectral fitting method described in Section 2.3. The quantities reported in columns (2), (3), (5), and (9) are as defined in Table 1. For the rest, from left to right, they are (1) the PRIMER-EXCELS ID, (4) the star-formation rate averaged over the previous 100 Myr (for measurements with median values $< 0.01 \text{ M}_\odot \text{ yr}^{-1}$, we report the 3σ upper limit; if the upper limit $< 0.01 \text{ M}_\odot \text{ yr}^{-1}$, we report this threshold as the upper limit), (6) cosmic time when half of the total stellar mass had been formed, (7) the redshift at which half of the total stellar mass had been formed, (8) the quenching redshift, at which $\text{sSFR} < 0.2/t_{\text{H}}$ is satisfied for the first time, and (10) the time span between when the galaxy had formed 10 per cent and 90 per cent of its total stellar mass. The galaxies’ celestial coordinates can be found in Table 1 of Carnall et al. (2024).

ID (1)	Redshift (2)	$\log_{10}(M_*/\text{M}_\odot)$ (3)	$\text{SFR} / \text{M}_\odot \text{ yr}^{-1}$ (4)	$\log_{10}(Z_*/\text{Z}_\odot)$ (5)	$t_{\text{form}} / \text{Gyr}$ (6)	z_{form} (7)	z_{quench} (8)	A_V / mag (9)	$\tau_{10-90} / \text{Myr}$ (10)
34495	3.7990 ± 0.0002	10.82 ± 0.03	11.57 ± 2.28	$-0.78^{+0.09}_{-0.12}$	$1.16^{+0.01}_{-0.01}$	$5.0^{+0.0}_{-0.0}$	$3.95^{+0.04}_{-0.04}$	$0.95^{+0.08}_{-0.08}$	236^{+12}_{-11}
39063	3.7021 ± 0.0002	10.46 ± 0.02	0.12 ± 0.14	$-0.12^{+0.11}_{-0.13}$	$1.15^{+0.01}_{-0.02}$	$5.0^{+0.1}_{-0.0}$	$4.39^{+0.17}_{-0.08}$	$0.07^{+0.04}_{-0.04}$	113^{+16}_{-33}
45981	3.0795 ± 0.0003	10.59 ± 0.02	< 0.01	$0.16^{+0.10}_{-0.09}$	$1.04^{+0.08}_{-0.08}$	$5.5^{+0.4}_{-0.3}$	$4.89^{+0.42}_{-0.44}$	$0.67^{+0.08}_{-0.07}$	111^{+383}_{-88}
50789	3.9889 ± 0.0002	11.00 ± 0.02	< 0.01	$-0.14^{+0.09}_{-0.08}$	$0.99^{+0.02}_{-0.02}$	$5.7^{+0.1}_{-0.1}$	$5.45^{+0.15}_{-0.28}$	$0.54^{+0.05}_{-0.04}$	31^{+39}_{-19}
52467	3.2394 ± 0.0003	10.52 ± 0.02	2.80 ± 0.50	$-0.21^{+0.10}_{-0.08}$	$1.38^{+0.01}_{-0.02}$	$4.3^{+0.1}_{-0.0}$	$3.49^{+0.04}_{-0.03}$	$0.16^{+0.04}_{-0.04}$	253^{+14}_{-12}
55410	3.1954 ± 0.0002	11.19 ± 0.02	< 1.29	$0.07^{+0.13}_{-0.09}$	$0.27^{+0.17}_{-0.14}$	$14.7^{+9.0}_{-4.4}$	$9.90^{+7.22}_{-3.19}$	$0.26^{+0.07}_{-0.06}$	270^{+253}_{-202}
55742 [†]	3.1972 ± 0.0005	10.04 ± 0.05	< 0.01	$-0.10^{+0.23}_{-0.17}$	$0.69^{+0.23}_{-0.22}$	$7.5^{+2.4}_{-1.5}$	$5.81^{+1.82}_{-0.79}$	$0.17^{+0.14}_{-0.10}$	220^{+470}_{-194}
57000	3.1945 ± 0.0004	10.81 ± 0.04	5.09 ± 2.43	$-0.00^{+0.13}_{-0.21}$	$1.40^{+0.01}_{-0.02}$	$4.3^{+0.1}_{-0.0}$	$3.45^{+0.11}_{-0.07}$	$1.01^{+0.09}_{-0.10}$	249^{+25}_{-33}
65915	4.3599 ± 0.0003	10.82 ± 0.02	< 0.01	$0.35^{+0.07}_{-0.18}$	$0.72^{+0.06}_{-0.08}$	$7.2^{+0.6}_{-0.4}$	$6.56^{+0.50}_{-0.49}$	$0.24^{+0.07}_{-0.06}$	80^{+235}_{-64}
106260	3.9788 ± 0.0005	10.82 ± 0.03	< 1.72	$0.12^{+0.11}_{-0.15}$	$1.01^{+0.03}_{-0.03}$	$5.6^{+0.1}_{-0.1}$	$5.17^{+0.35}_{-0.49}$	$1.54^{+0.10}_{-0.11}$	56^{+69}_{-42}
109760	4.6220 ± 0.0003	11.06 ± 0.02	< 0.01	$-0.73^{+0.07}_{-0.08}$	$0.48^{+0.06}_{-0.04}$	$9.8^{+0.7}_{-0.8}$	$6.94^{+0.69}_{-0.46}$	$0.95^{+0.07}_{-0.07}$	479^{+122}_{-239}
112990 [†]	3.8926 ± 0.0013	10.83 ± 0.05	63.60 ± 21.46	$-0.27^{+0.19}_{-0.27}$	$0.81^{+0.17}_{-0.12}$	$6.6^{+0.9}_{-0.9}$	*	$1.92^{+0.16}_{-0.17}$	1078^{+143}_{-273}
113667	3.9725 ± 0.0001	10.58 ± 0.02	< 0.01	$-0.87^{+0.09}_{-0.16}$	$1.00^{+0.02}_{-0.02}$	$5.6^{+0.1}_{-0.1}$	$5.43^{+0.13}_{-0.28}$	$0.10^{+0.06}_{-0.05}$	29^{+38}_{-18}
117560	4.6200 ± 0.0003	11.05 ± 0.02	< 0.09	$0.21^{+0.09}_{-0.13}$	$0.62^{+0.05}_{-0.04}$	$8.1^{+0.4}_{-0.5}$	$7.25^{+0.60}_{-0.78}$	$0.42^{+0.07}_{-0.06}$	93^{+187}_{-76}

[†] We obtain very large posterior uncertainties in most parameters, due to the low SNRs and poor Balmer line coverage of these EXCELS spectra. These two objects are therefore removed from all further analysis.

^{*} No measured z_{quench} value because the fitted star-formation history does not satisfy our quenched criterion of $\text{sSFR} < 0.2/t_{\text{H}}$ at any point.

3.2 Star-formation histories

3.2.1 The stellar mass vs stellar age relationship

In the left panel of Fig. 5, we plot the estimated stellar masses of the 12 massive quiescent galaxies against the cosmic times at which we estimate that half their stellar mass had formed (t_{form} , measured forwards from the Big Bang). Objects are coloured according to their observed redshifts. A tight negative relation is observed, where more massive galaxies formed the bulk of their stellar masses earlier than less massive galaxies. As discussed in Section 1, this is widely observed at lower redshift, and is known as “downsizing” or sometimes “archaeological downsizing” (e.g., Cowie et al. 1996; Pérez-González et al. 2008; Thomas et al. 2010).

Similar to earlier works at lower redshift (e.g., Gallazzi et al. 2014; Carnall et al. 2019a; Hamadouche et al. 2023), we follow the methods detailed in Hogg et al. (2010) to fit a linear relationship with intrinsic scatter in the vertical direction. For the mean relationship, we find

$$\left(\frac{t_{\text{form}}}{\text{Gyr}} \right) = 0.63^{+0.11}_{-0.14} - 1.58^{+0.38}_{-0.56} \log_{10} \left(\frac{M_*}{10^{11} \text{ M}_\odot} \right), \quad (1)$$

with an intrinsic scatter of $0.27^{+0.12}_{-0.07}$ Gyr. The mean relationship is shown in Fig. 5 as a cyan line, while its 1σ confidence region is marked with the shaded region. The pair of dotted cyan lines indicate the mean relationship \pm intrinsic scatter.

Notably, we find that the three most massive galaxies in our sample formed extremely early. Our measured SFH suggests that the most massive galaxy in our sample, PRIMER-EXCELS-55410 (otherwise known as ZF-UDS-7329), had formed half of its total stellar mass by $t_{\text{form}} = 0.27^{+0.17}_{-0.14}$ Gyr ($z_{\text{form}} = 14.7^{+9.0}_{-4.4}$). This is consistent with the red continuum shape, strong 4000Å break and weak Balmer absorption lines that can be seen for this object in Fig. 2. This result

is in good agreement with the results of previous studies that have focused on this object (Glazebrook et al. 2024; Carnall et al. 2024). It is also worth noting that the formation redshifts we infer for PRIMER-EXCELS-109760 and 117560 at $z = 4.62$ are consistent with the results of Carnall et al. (2024).

3.2.2 Archaeological downsizing and its evolution since $z \sim 5$

Our results in Fig. 5 provide a clear spectroscopic confirmation that the archaeological downsizing trend is already in place at $3 < z < 5$. We next compare the fitted t_{form} -mass relation from our sample with other results from the literature at $z > 1$ and $\log_{10}(M_*/\text{M}_\odot) > 10$ in the left panel of Fig. 6. The literature galaxies are obtained from Kriek et al. (2016), Schreiber et al. (2018), Belli et al. (2019), Forrest et al. (2020a,b), Valentino et al. (2020), Man et al. (2021), Carnall et al. (2023b), Kriek et al. (2024), Slob et al. (2024), Park et al. (2024), Jin et al. (2024), Setton et al. (2024), Nanayakkara et al. (2024), Antwi-Danso et al. (2025), Barrufet et al. (2025), Wu (2025), de Graaff et al. (2025), Weibel et al. (2025), and Skarbinski et al. (2025).

We begin by considering the work of Schreiber et al. (2018), who analysed ground-based spectroscopy for a sample of massive quiescent galaxies at $3 < z < 4$. Although probing massive quiescent galaxies at similar redshifts, our t_{form} -mass relation appears to be in tension with that obtained by Schreiber et al. (2018) (we plot the relationship derived by Hamadouche et al. 2023 from the Schreiber et al. 2018 results), who measured a flatter slope of $-0.73^{+0.64}_{-0.69}$ Gyr per dex in stellar mass, compared with our $-1.58^{+0.38}_{-0.56}$ Gyr per dex value. However, the stellar masses and ages in the Schreiber et al. (2018) sample were measured from fitting photometry alone given spectroscopic redshifts. This approach suffers from increased uncertainties and can lead to a flattening of the t_{form} -mass relation (see

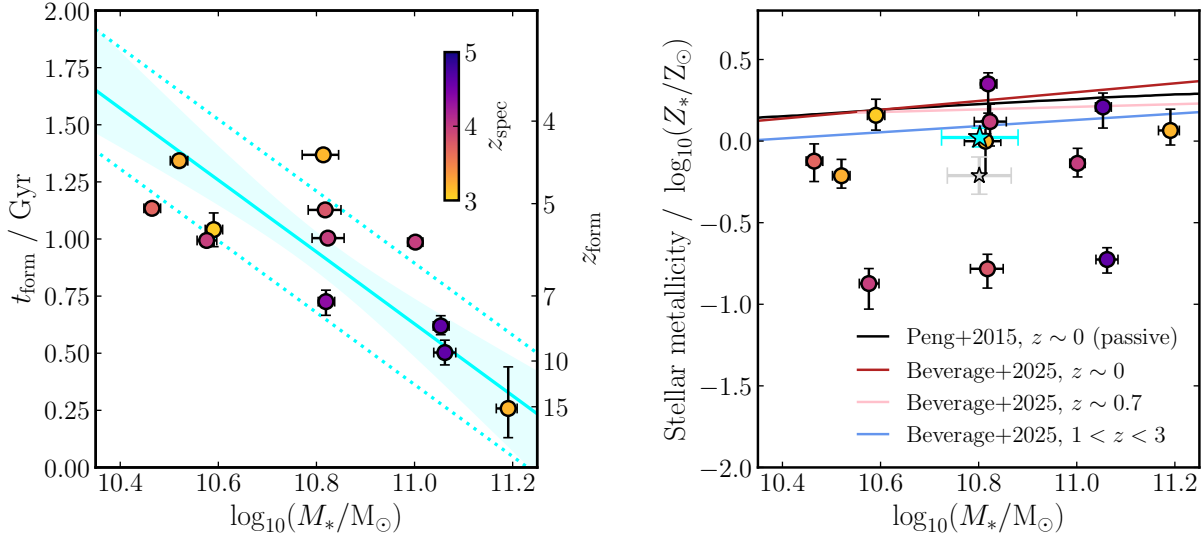


Figure 5. Relationships between stellar population properties for the 12 EXCELS $z > 3$ massive quiescent galaxies for which we obtain robust results. **Left:** Age of the Universe at which 50 per cent of the stellar mass in each galaxy had formed (t_{form}) as a function of stellar mass. Each galaxy is coloured according to its observed redshift (z_{spec}). We fit a straight line with intrinsic scatter to the tight correlation visible, which is represented by the light blue line and shaded region (Equation 1). The dotted light blue lines correspond to the $\pm 1\sigma$ intrinsic scatter we measure for the best-fit relation. **Right:** Stellar metallicity as a function of stellar mass, coloured in the same way as the left panel. The grey star shows the inverse-variance-weighted mean of our sample, with error bars showing the standard error on the mean. The cyan star shows the inverse-variance-weighted mean excluding the 3 very low metallicity objects (see Section 3.3). For comparison, we also show the stellar mass-metallicity relations of passive/quiescent galaxies from Peng et al. (2015) at $z \sim 0$ (light-weighted, black line) and Beverage et al. (2025) at $z \sim 0$ (red line), $z \sim 0.7$ (pink line) and $1 < z < 3$ (blue line).

section 6.1 of Carnall et al. 2019a). Additionally, due to the small sample sizes in both our study ($N = 12$) and Schreiber et al. (2018) ($N = 12$), the tension is not highly significant, at only 1.07σ .

Comparing to lower-redshift results, the slope of our t_{form} -mass relation shows excellent agreement with those measured at the cosmic noon epoch ($1 \lesssim z \lesssim 3$) from spectroscopic data. Using ultra-deep spectroscopy for 114 massive quiescent galaxies from the VANDELS survey, Hamadouche et al. (2023) found quiescent galaxies at $1 < z < 1.3$ exhibit an age-mass slope of $-1.20^{+0.28}_{-0.27}$ Gyr per dex in stellar mass, consistent with our higher-redshift result. Hamadouche et al. (2023) also measured an age-mass slope for the 23 quiescent galaxies reported by Belli et al. (2019) at $1.5 < z < 2.5$, derived from Keck-MOSFIRE spectroscopy. Their result is -1.73 ± 0.40 Gyr per dex in stellar mass, which is also within 1σ of our measured slope in Equation 1.

The analysis of Carnall et al. (2019a) (an earlier version of that presented by Hamadouche et al. 2023) also concluded that this $\simeq 1.5$ Gyr per dex slope appears to be consistent with the results of Gallazzi et al. (2005) at $z \simeq 0.1$ and Gallazzi et al. (2014) at $z \simeq 0.7$, however substantial methodological differences (e.g., the use of light-weighted, rather than mass-weighted ages) makes this comparison more challenging.

The broadly parallel nature of these age-mass relationships across $0 < z < 5$ indicates that, with decreasing redshift, the increase in mean quiescent galaxy formation time is largely independent of stellar mass. Given that our results show clear evidence for the archaeological downsizing trend already being in place by $z \sim 4$, only ~ 1.5 Gyr after the Big Bang, some of the proposed drivers of downsizing discussed in Section 1, such as environmental effects and dry mergers, are unlikely to have had enough time to make a significant contribution (but see Ito et al. 2025).

Finally, it is worth noting that our sample of massive quiescent galaxies at $3 < z < 5$ overlaps in the left panel of Fig. 6 with the

galaxies at $z \simeq 1$ that formed at the earliest times, suggesting that a fraction of massive quiescent galaxies at $3 < z < 5$ will remain quiescent for > 3 Gyr (and perhaps much longer), becoming ancient relics by $z \lesssim 1$ (e.g., Ferré-Mateu et al. 2017; Spinello et al. 2021).

3.2.3 Archaeological downsizing in simulations

The archaeological downsizing trend is also of interest because it can be readily compared with predictions from cosmological simulations (e.g., Nelson et al. 2018; Carnall et al. 2019a; Lovell et al. 2023). This provides a useful additional constraint to number-density comparisons, being strongly dependent on the physical process that gives rise to quenching. In Fig. 7, we compare our observed age-mass relationship with those predicted from the COLIBRE cosmological hydrodynamic simulation (Schaye et al. 2025; Chaikin et al. 2025), taken from Chandro-Gómez et al. (2025), for objects selected in the same way as our observational sample. COLIBRE is notable for accurately reproducing the number density of massive quiescent galaxies at $3 < z < 5$ (Chandro-Gómez et al. 2025), whereas many other simulations under-predict the abundance of such objects (e.g., Lagos et al. 2025; Stevenson et al. 2025).

It can be seen from Fig. 7 that COLIBRE broadly predicts flat age-mass relationships at all redshift bins between $z = 2$ and $z = 4$, but the simulation suffers from a lack of statistics at the high-mass end at the highest redshifts. In contrast, our observed relation and those from Schreiber et al. (2018) and Belli et al. (2019) all exhibit steeper slopes. We therefore report tentative evidence that, although COLIBRE is broadly able to reproduce the observed number densities of massive quiescent galaxies at $z > 2$, there is some evidence that the observed stellar ages are not yet well reproduced. It has been previously noted that other simulations also struggle to reproduce the oldest $z > 3$ quiescent galaxies, instead producing exclusively young objects (e.g., Hartley et al. 2023; Weller et al. 2025).

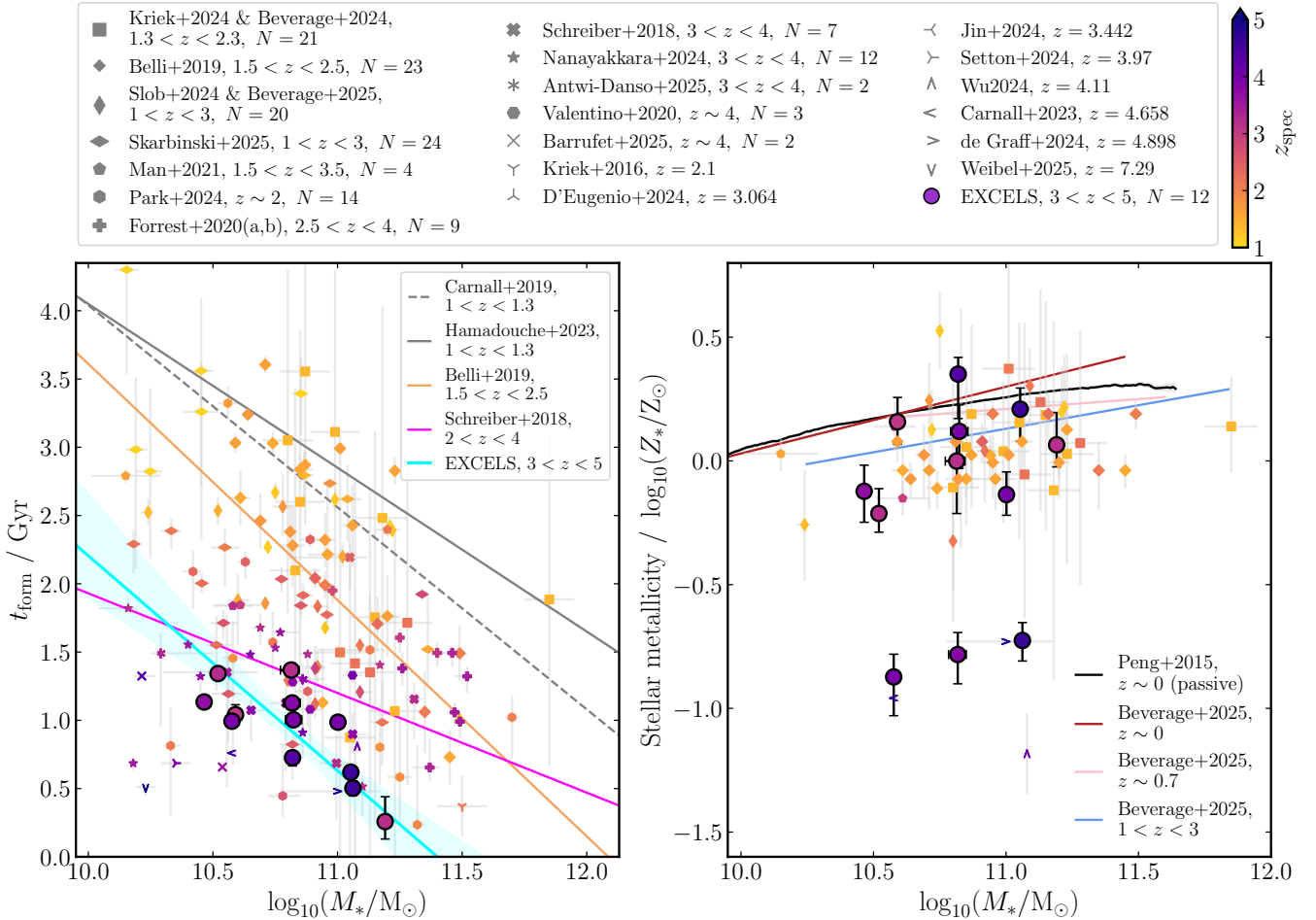


Figure 6. The stellar population properties for our sample of massive quiescent galaxies, as shown in Fig. 5, placed in literature context. In both panels, we have included individual massive quiescent galaxies reported in the literature at $z > 1$ (see Sections 3.2.2 and 3.3 for full lists of references). **Left:** Age of the Universe at which 50 per cent of the stellar mass in each galaxy had formed (t_{form}) as a function of stellar mass. The cyan line and shaded region is our best-fit relation to the EXCELS sample, as shown in Fig. 5. We also plot the mean relations from Hamadouche et al. (2023) (grey solid line) and Carnall et al. (2019a) (grey dashed line) at $1 < z < 1.3$. In addition, we plot the mean relations measured by Hamadouche et al. (2023) using samples from Belli et al. (2019) at $1.5 < z < 2.5$ (orange line) and Schreiber et al. (2018) at $3 < z < 4$ (magenta line). Our galaxies follow a mass-age sequence, with a slope consistent with those reported for spectroscopic samples at $1 < z < 2.5$. The Schreiber et al. (2018) relationship is shallower, probably due to their SFHs being derived purely from photometric data. **Right:** Stellar metallicity as a function of stellar mass. We again show the mean relationships plotted in Fig. 5, as well as individual-object results from a range of studies. We see no clear mass-metallicity relation in our relatively small sample. However, excluding our 3 lowest-metallicity objects, our results are consistent with the literature at $1 < z < 3$. Note that compared to the previous figures, the colour map has been expanded to cover the redshift range $1 < z < 5$.

3.2.4 Star-formation-history shapes

We show the fitted SFHs of all 12 EXCELS galaxies for which we obtain a good fit in Fig A1. It can be seen that these objects generally experienced extremely rapid assembly of their stellar mass. The assembly duration, which we measure via the time span between when the galaxy had formed 10 per cent and 90 per cent of its total stellar mass (τ_{10-90}), has a mean value of 203 ± 7 Myr. Only 1/12 of our galaxies, 109760, has a posterior median assembly duration, $\tau_{10-90} > 300$ Myr. Such rapid assembly requires peak SFRs of several hundred solar masses per year, a level that is comparable to the SFRs of the most extreme submillimetre galaxies at the redshifts our objects formed (e.g., Michałowski et al. 2017; Liu et al. 2025; Bing et al. 2025).

3.2.5 Implications for quiescent galaxies at higher redshifts

The age-mass relationship we report in Equation 1 has interesting implications for extremely early massive quiescent galaxies, such as the object RUBIES-UDS-QG-z7 reported by Weibel et al. (2025) at $z = 7.3$, which appears to have formed its stellar mass of $\log_{10}(M_*/M_\odot) \simeq 10.2$ at $z \simeq 8 - 9$. Whilst our sample is only mass complete at $\log_{10}(M_*/M_\odot) > 10.4$, and does not contain galaxies at lower stellar masses, the clear implication of our result is that massive quiescent galaxies at $3 < z < 5$ with $\log_{10}(M_*/M_\odot) \gtrsim 10$ have formed and quenched very recently. The only objects we find in our sample with similar t_{form} to RUBIES-UDS-QG-z7 all have $\log_{10}(M_*/M_\odot) \gtrsim 11$. This implies that RUBIES-UDS-QG-z7 will likely remain quiescent for only a short duration, before rejuvenating.

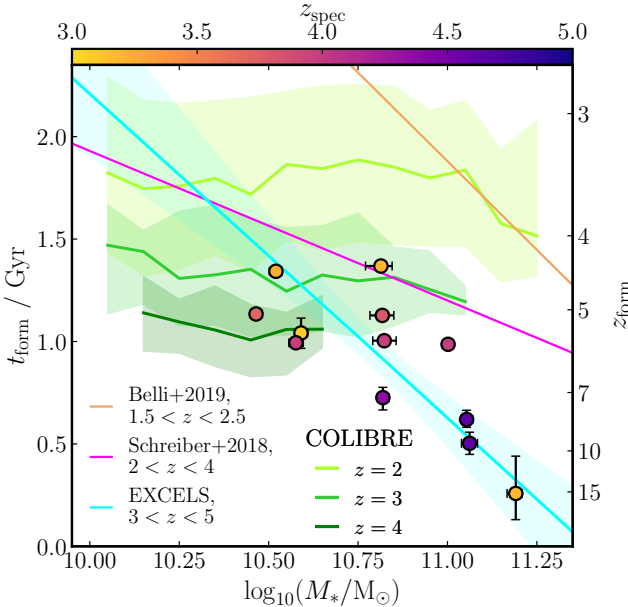


Figure 7. A comparison of observational age-mass relationships for massive quiescent galaxies to predictions from simulations. The vertical axis shows the age of the Universe at which galaxies formed the 50th percentile of their stellar mass. We plot the individual-galaxy EXCELS results (circles), our best fit age-mass relationship (cyan) and the relationships measured by Hamadouche et al. (2023) from the lower redshift samples of Belli et al. (2019) (orange) and Schreiber et al. (2018) (magenta) in similar styles to Fig. 6. The Chandro-Gómez et al. (2025) relationships predicted by the COLIBRE simulation at $z = 2$, $z = 3$ and $z = 4$ are shown in shades of green, with shaded regions indicating the 16th to 84th percentile ranges.

3.3 Stellar metallicities

In the right panel of Fig. 5 we plot our measured stellar masses against our measured stellar metallicities. We also show several median relationships from the literature. The black line shows the result of Peng et al. (2015), measured from local Sloan Digital Sky Survey (SDSS) quiescent galaxies. The other three relationships are those reported by Beverage et al. (2025). Their $z \sim 0$ line, shown in red, is derived using individual galaxy results from Zhuang et al. (2023), again based on SDSS data. The $z \sim 0.7$ line, shown in pink, is derived from the LEGA-C survey results of Beverage et al. (2023). The blue $1 < z < 3$ line is derived from SUSPENSE survey data (Slob et al. 2024). A more detailed literature comparison, including results for individual objects obtained from Belli et al. (2019), Man et al. (2021), Carnall et al. (2023b), Beverage et al. (2024, 2025)³, Wu (2025), and de Graaff et al. (2025), is presented in the right panel of Fig. 6.

We observe larger scatter in our sample compared to galaxies at lower redshifts, in particular towards far lower metallicities. The inverse-variance-weighted mean metallicity we measure for our sample, marked with a grey star in Fig. 5, is $\log_{10}(Z_{*,\text{mean}}/Z_\odot) = -0.21 \pm 0.11$. This lies below the $1 < z < 3$ relation from Beverage et al. (2025), however this is primarily driven by the three outlying metal-poor galaxies in our sample. If we exclude these three galaxies, the distribution of the remaining objects in our sample ap-

pears to agree well with the Beverage et al. (2025) $1 < z < 3$ relation. The inverse-variance-weighted mean metallicity excluding the three low-metallicity objects, which is shown with a cyan star in Fig. 5, is $\log_{10}(Z_{*,\text{mean}}/Z_\odot) = 0.02 \pm 0.06$.

The three galaxies with significantly lower metallicity estimates, 34495, 109760 and 113667, are consistent with the strongly sub-solar metallicities that have recently been reported for several massive quiescent galaxies observed at $z > 4$ (Carnall et al. 2023b; de Graaff et al. 2025; Wu 2025). Combined with the examples in the literature, these galaxies might represent a new type of evolutionary path for early massive quiescent galaxies that rapidly formed and quenched while maintaining substantially sub-solar chemical abundances. However, it is challenging to explain why no such objects appear to be found at lower redshift (though it is possible these galaxies will later become more metal-rich by rejuvenating or accreting more metal-rich stars through mergers).

All three low-metallicity galaxies in our sample have moderately young stellar populations (≈ 500 Myr since quenching), which is also true for the literature examples cited above. The spectrum of 113667 in particular has a clear triangular shape and very deep Balmer absorption lines, closely resembling that of an A-type star. In this context, it seems plausible that these anomalously low stellar metallicity results are instead due to an inadequacy of current low metallicity stellar population models in this relatively poorly explored age regime. We have tested re-fitting these three objects whilst requiring higher stellar metallicities, and confirm that, whilst this results in a lower quality of fit, the stellar ages of these objects are not strongly affected, and the effect on the relationship presented in Equation 1 is minimal.

Next, in the right panel of Fig. 6, we place our results from Fig. 5 in the context of a large number of individual stellar metallicity measurements for spectroscopically observed $\log_{10}(M_*/M_\odot) > 10$ quiescent galaxies at $z > 1$ from the literature. In general, our stellar metallicity results appear to support a picture in which the quiescent stellar mass-metallicity relation shifts only very modestly towards lower metallicities at earlier times.

When comparing our results to the literature relationships shown, it is important to note that they have been measured via different methods. The Peng et al. (2015) relation is based on values first measured by Gallazzi et al. (2005), who measured light-weighted metallicities from a selection of Lick indices, spectral breaks and absorption features. The difference between light-weighted metallicities and mass-weighted metallicities in quiescent galaxies is however estimated to be < 0.1 dex (Trussler et al. 2020).

The Bruzual & Charlot (2003) models used in our primary fitting approach assume scaled-solar elemental abundances, whereas high-redshift galaxies with rapid formation timescales are expected to be significantly α -enhanced (e.g., Thomas et al. 2005; Kriek et al. 2016; Kobayashi et al. 2020). In Beverage et al. (2025), the authors compared stellar metallicities measured assuming scaled-solar chemical abundances against measurements from fitting the abundances of individual elements separately (albeit assuming a simpler treatment of SFH, dust attenuation and nebular emission). The authors found that metallicity values from full spectral fitting could be up to $\approx 0.8 - 0.9$ dex lower than values derived from measuring individual abundances (see the middle panel of their fig. 6). This could also provide an explanation for the three very low stellar metallicity objects in our sample, however unfortunately the Conroy et al. (2018) stellar population models used by Beverage et al. (2025) are only available for ages > 1 Gyr.

The general lack of available models for α -enhanced stellar populations covering broad age and wavelength ranges has long limited

³ Beverage et al. (2024) presents the same sample as Kriek et al. (2024), while Beverage et al. (2025) presents the same sample as Slob et al. (2024).

progress in this area, however several groups have recently developed new sets of α -enhanced stellar population models (e.g., [Knowles et al. 2021, 2023](#); [Byrne et al. 2025](#); [Park et al. 2025](#)). We therefore explore fitting our sample with stellar models that allow flexibility in elemental abundance patterns in Section 4.

3.4 AGN contributions and black-hole masses

Only one galaxy in our sample, 34495, is best fitted with a significant AGN contribution. We estimate a broad H α flux of $f_{\text{H}\alpha, \text{broad}} = 1.5 \pm 0.3 \times 10^{-17}$ erg s $^{-1}$ cm $^{-2}$ and full width at half maximum (FWHM) of 9500^{+2000}_{-1600} km s $^{-1}$. This broad-line width is similar to that measured for the quiescent galaxy GS-9209 at higher redshift ([Carnall et al. 2023b](#)), as well as some $z \approx 6$ quasars (e.g., [Chehade et al. 2018](#); [Onoue et al. 2019](#)).

From our measured broad H α flux for 34495, we use the relation in equation 6 of [Greene & Ho \(2005\)](#) to estimate a black-hole mass of $\log_{10}(M_{\text{BH}}/M_{\odot}) = 8.5^{+0.3}_{-0.2}$, which corresponds to a black-hole-to-stellar mass ratio of $M_{\text{BH}}/M_{*} = 0.4^{+0.3}_{-0.2}$ per cent. Interestingly, this mass ratio is consistent with the black-hole-to-bulge-mass ratios measured from local early type galaxies by [Kormendy & Ho \(2013\)](#), and does not follow the trend towards heightened mass ratios recently reported for many $z > 4$ galaxies (e.g., [Pacucci & Loeb 2024](#); [Maiolino et al. 2024](#)). This is consistent with 34495 going on to form the bulge component of a local galaxy with little further evolution.

The black-hole-to-stellar mass ratio we measure for 34495 is also lower than the ratio recently derived for the similar object GS-9209 ([Carnall et al. 2023b](#)) at $z = 4.66$, which has a higher black-hole-to-stellar mass ratio of $1.1^{+0.4}_{-0.3}$ per cent. Whilst this relationship is known to have considerable scatter, and estimates at these redshifts are still scarce, our new result for 34495 combined with the previous GS-9209 result suggests that the average black-hole-to-stellar mass ratio for massive quiescent galaxies at $z \gtrsim 4$ may be similar to the 0.8 per cent average black-hole-to-bulge mass ratio derived by [McLure et al. \(2006\)](#) for the most massive elliptical galaxies at $z = 2$.

4 ALPHA ENHANCEMENT

Alpha (α) elements are elements that are mainly produced through the α process in stellar nucleosynthesis, such as C, O, Ne, Mg, Ca and Si. They are released into the interstellar medium (ISM) in greater quantities through Type II supernovae, while Fe-peak elements are released mainly through Type Ia supernovae (e.g., [Maiolino & Manucci 2019](#)). The different onset timescales of these two processes after a starburst (Type II ≈ 10 Myr; Type Ia ≈ 1 Gyr, see [Maoz et al. 2012](#)) mean that α -abundance is a powerful tracer of the duration of past star formation (e.g., [Thomas et al. 2010](#)). Our fiducial results presented in Section 3 assume scaled-solar stellar abundances, however early galaxies have been shown to be more α -abundant compared to other elements than is true for the Sun, or ‘ α -enhanced’ ([Steidel et al. 2016](#); [Topping et al. 2020](#); [Cullen et al. 2021](#); [Zhuang et al. 2023](#); [Stanton et al. 2024](#); [Beverage et al. 2025](#); [Shapley et al. 2025](#)). Assuming scaled-solar α -abundances could potentially bias our stellar age and metallicity results due to degeneracies between these parameters ([Vazdekis et al. 2015](#); [Choi et al. 2019](#)). Hence, it is important to explore α -enhancement in our galaxies and its impact on the quality of our measured galaxy properties.

4.1 Variable α -abundance fitting implementation

Metal absorption features in the rest-frame optical typically increase in strength with increasing stellar population age (as well as metallicity), therefore these features are not typically visible in the atmospheres of hot O, B and A-type stars. Thus, in this section we use only galaxies for which the posterior median time since half of their stellar mass formed exceeds 500 Myr (i.e., $t_{\text{H}}(z) - t_{\text{form}} > 500$ Myr) in our fiducial [Bruzual & Charlot \(2003\)](#) fitting run (see Table 2).

To ensure faint metal absorption features in the spectra are detectable so that $[\alpha/\text{Fe}]$ can be constrained, we also impose a threshold on SNR, requiring SNR per $\text{\AA} > 6$ averaged over $5100 < \lambda_{\text{rest}} < 6400$ \AA . For 65915, the Mg absorption complex at $\lambda_{\text{rest}} \approx 5170$ \AA was not observed due to a detector gap. As this feature is a key indicator of α -abundance ([Thomas et al. 2003](#); [Byrne et al. 2022](#); [Knowles et al. 2023](#); [Park et al. 2025](#)), we also exclude this galaxy. Therefore, in this section we repeat our full spectral fitting with variable $[\alpha/\text{Fe}]$ abundance (−0.2 to 0.6 dex) for 6 galaxies: 45981, 50789, 55410, 109760, 113667 and 117560.

We conduct 5 separate fitting runs allowing α -abundance to vary, described in the following sub-sections, using both the BPASS and SMILES models, which we implement within the BAGPIPES code, and the sMILES and [Conroy et al. \(2018\)](#) models using the `alf-alpha` code. A summary of these 5 fitting approaches is provided in Table 3.

In addition to the 6 massive quiescent galaxies at $3 < z < 5$, we also repeat the 5 fitting configurations on SNR per $\text{\AA} > 500$ spatially stacked spectra of two local ($z < 0.05$) quiescent galaxies from the SDSS MaNGA survey ([Bundy et al. 2015](#)) as controls. Stacking is performed via an unweighted sum of the flux column for each spaxel, while the uncertainties are summed in quadrature. MaNGA-11835-9101 is chosen as a classical ‘red and dead’ old elliptical galaxy, which has no measurable star formation at least within the past 3 Gyr. MaNGA-12514-3702 is selected as a post-starburst galaxy in [Leung et al. \(2024\)](#), which underwent a period of increased star formation at ≈ 1 Gyr in lookback time, and subsequently rapidly quenched. The post-starburst nature of this object provides a useful analogue to the early massive quiescent galaxies in our EXCELS sample.

4.1.1 Adding variable α -abundance stellar models to BAGPIPES

We adopt two SSP libraries that provide models with variable $[\alpha/\text{Fe}]$ abundances. Based on the same stars as the empirical MILES spectral library, the sMILES SSP library provides semi-empirical model spectra over the rest-frame wavelength range from 3540 – 7410 \AA , ranging from $[\alpha/\text{Fe}] = -0.2$ to $+0.6$ dex ([Knowles et al. 2023](#)). The sMILES models provide a good match to our fiducial [Bruzual & Charlot \(2003\)](#) models because of their matching wavelength range and spectral resolution (FWHM = 2.5 \AA). Additionally, both were constructed from the same suite of empirical stellar spectra. However, the sMILES library lacks the broader rest-frame UV and IR coverage of the [Bruzual & Charlot \(2003\)](#) models, which drastically limits the number of photometric points that can be included along with the EXCELS spectroscopy for each fit. This has the potential to introduce biases in the measurements of SFHs and other physical properties (e.g., [Pforr et al. 2012](#); [Hunt et al. 2019](#)).

The second model library is version 2.3 of Binary Populations and Spectral Synthesis (BPASS), also ranging from $[\alpha/\text{Fe}] = -0.2$ to $+0.6$ dex ([Byrne et al. 2022, 2025](#)). Due to their completely theoretical nature, these models span the full wavelength range probed by our *JWST+HST* photometry, as well as our EXCELS spectroscopy.

We re-scale both SSP libraries to the [Asplund et al. \(2009\)](#) solar abundances (see Appendix B), and implement them in BAGPIPES,

including the ability to vary $[\alpha/\text{Fe}]$ as a free parameter. The prior used is uniform within $-0.2 < [\alpha/\text{Fe}] < 0.6$. All of the other fitting parameters and priors are as described in Table 1.

By default, BAGPIPES does not include CLOUDY photoionisation models that vary in $[\alpha/\text{Fe}]$ abundance. As we do not fit any galaxies that show noticeable current or recent ($\lesssim 100$ Myr timescale) star formation according to their estimated SFHs from our fiducial fits (see Section 3.1 and Fig. A1), we do not explore the production of α -enhanced CLOUDY models in this work (though this is something we plan to address in future work). Although we lack photoionisation models that vary in $[\alpha/\text{Fe}]$ consistently with the SSP libraries, we opt to include photoionisation models computed from SSPs without $[\alpha/\text{Fe}]$ variation. Fits based on sMILES SSPs use nebular models computed from Bruzual & Charlot (2003) models. Fits based on BPASS version 2.3 use nebular models computed from the earlier BPASS version 2.2.1. Their inclusion is only to disfavour solutions with very young stellar ages during SED fitting. Because we only fit the 6 galaxies with no current or recent star formation within 500 Myr, the impact of not using photoionisation models that vary in $[\alpha/\text{Fe}]$ is negligible.

For both sets of models we fit our EXCELS spectra over the same $3540 - 7350$ Å wavelength range and with the same emission-line masking as described in Section 2.3. In addition, we also mask the calcium H and K lines at $\lambda_{\text{rest}} \approx 3950$ Å for all 5 rounds of fitting with variable $[\alpha/\text{Fe}]$. These lines are useful tracers of stellar calcium abundance, which can be used to measure α -enhancement. However, calcium in the ISM can also provide a substantial contribution to these lines (e.g., Murga et al. 2015), which has the potential to bias our measurements of $[\alpha/\text{Fe}]$.

4.1.2 Fitting with $\text{Alf-}\alpha$

Another commonly used method to constrain α -enhancement is by measuring individual elemental abundances using the Absorption Line Fitter code (`alf`, Conroy & van Dokkum 2012; Conroy et al. 2018). However, the stellar models used in `alf` do not extend below an age of 1 Gyr, making it unsuitable for some of the galaxies in our sample. Instead, we adopt the more-recently developed $\text{Alf-}\alpha$ code (Beverage et al. 2025) based on `alf`, which also includes the sMILES SSP library as well as the standard Conroy et al. (2018) `alf` stellar models. Since historically most works in the literature have used `alf` with the Conroy et al. (2018) models to measure individual elemental abundances, for completeness we use $\text{Alf-}\alpha$ to fit both the sMILES models and the Conroy et al. (2018) models to our emission-line-masked EXCELS spectra. The $\text{Alf-}\alpha$ code also includes the ability to produce predictions from the Conroy et al. (2018) models for stellar populations younger than 1 Gyr through extrapolation. We opt to use this functionality, however it should be noted that this comes with the potential for significantly increased systematic uncertainties.

When fitting with the sMILES models, we pass $\text{Alf-}\alpha$ the full MILES-wavelength-range EXCELS spectra after masking emission lines, as described in Section 2.3 (the $\text{Alf-}\alpha$ code does not include the ability to fit photometric data). With these models, $\text{Alf-}\alpha$ assumes a relatively simple galaxy model with 10 free parameters. These are redshift, stellar age (assuming a single-burst SFH model), total stellar metallicity ($\log_{10}(Z_*/Z_\odot)$), $[\alpha/\text{Fe}]$, stellar velocity dispersion, emission line strengths for the Balmer lines (assuming case-B recombination) and $[\text{O III}]$, velocity offset and dispersion of the emission lines, and a white noise scaling term (similar to s in Table 1).

When fitting with the Conroy et al. (2018) models, we limit the fitted wavelength range to $4000 - 6400$ Å and $8000 - 8800$ Å in the

rest frame, following Conroy et al. (2014), which we call the “`alf` range”. The fit assumes a single burst SFH model and has 20 free parameters, including all parameters listed above in the `alf- α` fit using sMILES except for $[\alpha/\text{Fe}]$, which is replaced with individual abundances for 10 elements, including Mg and Fe, and an additional varying effective temperature for the hot star component (Conroy et al. 2018). To provide a close comparison to this round of fitting, we also repeat our BAGPIPES fits using the BPASS library, this time limiting our EXCELS spectra to the `alf` range. This also probes the effects of fitting different rest-frame wavelength ranges on the measured properties.

4.2 Variable α -abundance fitting results

In Fig. 8, we compare the estimated values of $\log_{10}(Z_*/Z_\odot)$, $[\text{Fe}/\text{H}]$, $[\text{Mg}/\text{H}]$, $[\text{Mg}/\text{Fe}]$ and time since quenching (t_{sq}) from the 5 fitting configurations described in Section 4.1 and summarised in Table 3. We calculate the time since quenching as $t_{\text{sq}} = t_{\text{H}}(z_{\text{obs}}) - t_{\text{H}}(z_{\text{quench}})$, where t_{H} is the Hubble time, z_{obs} is the redshift at which the galaxy is observed, and z_{quench} is the redshift at which the galaxy first fell below $\text{sSFR} = 0.2/t_{\text{H}}(z)$. For fits using the sMILES library, we assume $[\text{Mg}/\text{H}] = [\alpha/\text{H}]$ and $[\text{Mg}/\text{Fe}] = [\alpha/\text{Fe}]$. For fits using the BPASS library, we perform linear interpolation based on an abundance table to obtain $[\text{Fe}/\text{H}]$, $[\text{Mg}/\text{H}]$ and $[\text{Mg}/\text{Fe}]$ (see Appendix B). In all panels, the fitting configurations are colour-coded according to the legend at the top of the figure, with full details given in Table 3. Symbols mark the posterior median values, while the error bars mark the 16th–84th percentile ranges of the posterior distributions. Where applicable, the vertical dashed lines mark the posterior median estimates from the fiducial BAGPIPES Bruzual & Charlot (2003) fits from Section 3 with no variable α -abundance. All results are homogenised onto to the Asplund et al. (2009) solar abundance scale following the methods described in Appendix B.

4.2.1 High-redshift sample

In the three left-most columns in Fig. 8, significant disagreements between the different fitting configurations can be seen. Estimated $\log_{10}(Z_*/Z_\odot)$, $[\text{Fe}/\text{H}]$, and $[\text{Mg}/\text{H}]$ values for the same $z > 3$ galaxy can vary by as much as 2 dex between the configurations (e.g., 113667). It can be seen that fits based on different SSP libraries lead to significantly varying results. For example, results from both BPASS configurations (blue and orange) for 45981 and 55410 consistently show lower $\log_{10}(Z_*/Z_\odot)$, $[\text{Fe}/\text{H}]$ and $[\text{Mg}/\text{H}]$ estimates than the other configurations, as well as our fiducial Bruzual & Charlot (2003) estimate for $\log_{10}(Z_*/Z_\odot)$. This is consistent with the results of Byrne & Stanway (2023), who find significantly varying strengths for the same metal absorption lines at the same ages and metallicities in different model libraries, attributing this to the different libraries adopting varying ingredients and assumptions, such as stellar isochrones and spectral templates. This is also consistent with recent results at $z \approx 2$ from Jafaryazani et al. (2025).

In addition, fits performed on different wavelength ranges of the observed spectra give substantially different results in some cases, even when fitting with the same model library. In Fig. 8, for 45981, 50789, 113667 and 117560, results from the BAGPIPES-BPASS configuration fitting the `alf` wavelength range (blue) tend to show significantly lower $\log_{10}(Z_*/Z_\odot)$ than the BAGPIPES-BPASS configuration fitting the MILES wavelength range (orange), along with lower $[\text{Fe}/\text{H}]$ and $[\text{Mg}/\text{H}]$, and slightly older ages (e.g., 50789). The direction of these differences is consistent with the well-documented

Table 3. The configurations of the 5 fitting runs we adopt to measure the stellar α -abundances of our massive quiescent galaxies, detailed in Section 4.1. For the BAGPIPES run using the sMILES SSP library, due to the limited wavelength range of sMILES, only photometric points with filter profiles that lie fully within the MILES wavelength range could be included, which is typically 1-2 NIRCam band(s). The “colour” column refers to the colours shown in Figs 8 and 9.

Fitting code	SSP library	SFH model	Wavelength range (rest frame)	Photometry	Colour
$\alpha\text{lf}\alpha$	Conroy et al. (2018) (VCJ)	single burst	alf range: 4000 – 6400Å & 8000 – 8800Å	None	black
BAGPIPES	BPASS v2.3	double power law	alf range: 4000 – 6400Å & 8000 – 8800Å	full <i>JWST+HST</i>	blue
BAGPIPES	BPASS v2.3	double power law	MILES range: 3540 – 7410Å	full <i>JWST+HST</i>	orange
BAGPIPES	sMILES	double power law	MILES range: 3540 – 7410Å	<i>JWST+HST</i> if in range	lime
$\alpha\text{lf}\alpha$	sMILES	single burst	MILES range: 3540 – 7410Å	None	magenta

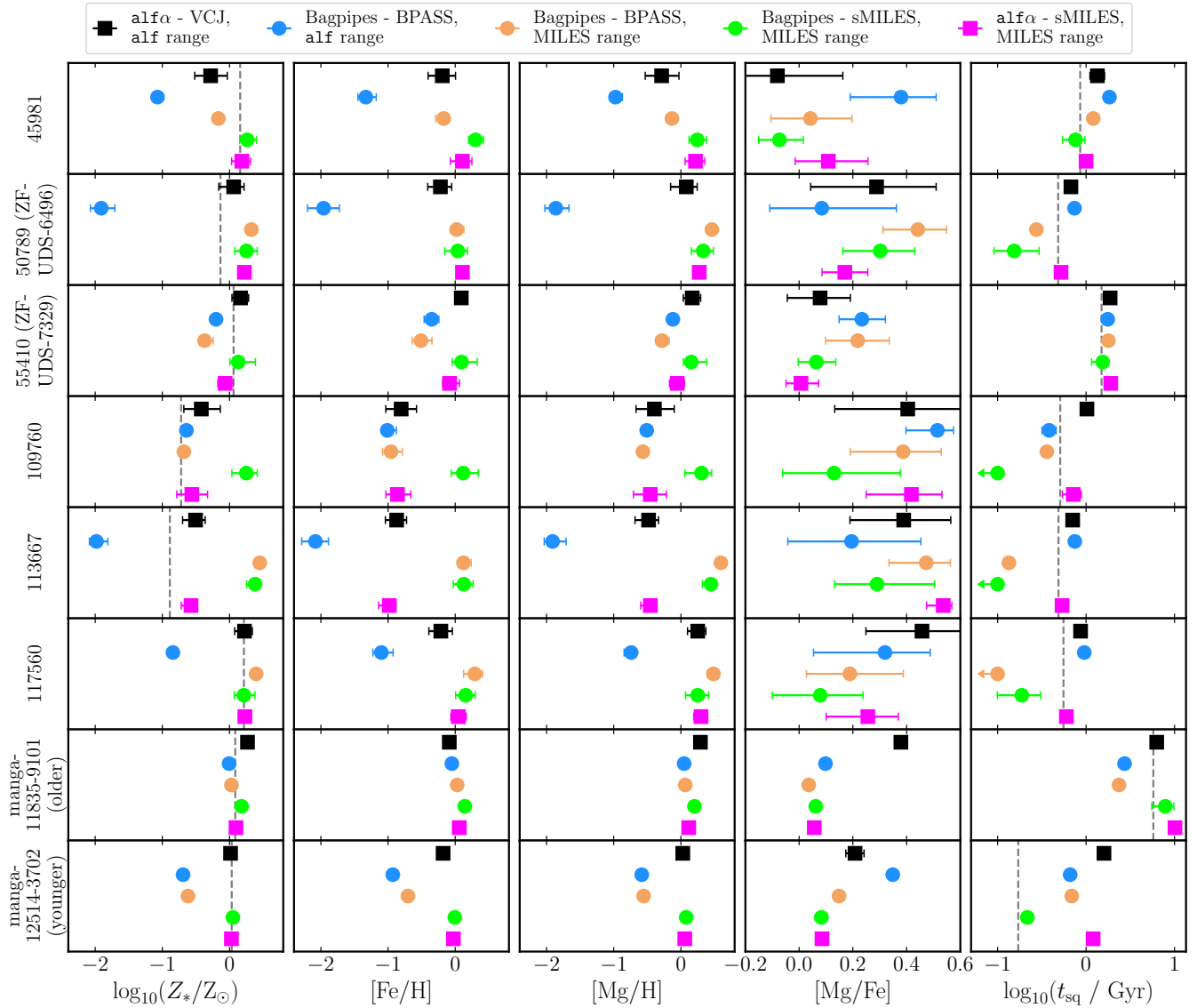


Figure 8. A comparison of the stellar properties estimated from our 5 different $[\alpha/\text{Fe}]$ -varying fitting configurations (see Section 4.1 and Table 3) for 6 massive quiescent galaxies from our sample and 2 MaNGA low-redshift control objects. Galaxies are ordered in rows, and stellar properties are ordered in columns. From left to right, columns show the total stellar metallicity, $[\text{Fe}/\text{H}]$, $[\text{Mg}/\text{H}]$, $[\text{Mg}/\text{Fe}]$ and the lookback time to the point at which the galaxy quenched (defined as when $\text{sSFR} < 0.2/t_{\text{H}}$ is satisfied for the first time). All abundances have been adjusted to the Asplund et al. (2009) scale (see Appendix B). Within each panel, the marker and error bars denote the 16th, 50th and 84th percentiles of the corresponding posterior distribution. The correspondence between colours and fitting runs is given in the figure legend and also in Table 3. Circles (squares) mark results from $\alpha\text{lf}\alpha$ (BAGPIPES) fits. Vertical dashed lines mark the posterior median estimate from the fiducial fits using the Bruzual & Charlot (2003) stellar models (not marked in the $[\text{Fe}/\text{H}]$, $[\text{Mg}/\text{H}]$ and $[\text{Fe}/\text{Mg}]$ panels because these abundances were forced to follow the total stellar metallicity in the fiducial fits). The x-axis limits of the $[\text{Mg}/\text{Fe}]$ column are set to $[-0.2, 0.6]$, the limits of all BAGPIPES fits. Instances where the posterior estimated SFH is not quenched at $z = z_{\text{obs}}$ have $\log_{10}(t_{\text{sq}}/\text{Gyr})$ marked as an upper limit at -1 .

age-metallicity degeneracy in spectral fitting, where an older, more metal-poor stellar population can produce a similar spectrum to a younger, more metal-rich stellar population (e.g., [Worley 1994](#); [Conroy 2013](#)). These differences are potentially attributable to the fact that the light from different stellar populations dominate at different wavelengths. Therefore, different portions of the galaxy spectrum are preferentially sensitive to different stellar populations, as well as different elemental abundances, due to the inclusion of different spectral features ([Conroy & Gunn 2010](#); [Conroy 2013](#); [Baldwin et al. 2018](#)).

As can be seen in the second column from the right in Fig. 8, the $[\text{Mg}/\text{Fe}]$ values we estimate for the early massive quiescent galaxies are typically highly uncertain for all fitting configurations. The best constraints are obtained for 55410, the galaxy with the highest SNR in our high-redshift sample. We also observe substantial scatter in estimated $[\text{Mg}/\text{Fe}]$ across the different fitting configurations, however, due to the large uncertainties, the different $[\text{Mg}/\text{Fe}]$ estimates typically agree within their 1σ uncertainties.

For 109760 (4th row from top in Fig. 8), good agreement is achieved among all fitting configurations except BAGPIPES-sMILES (lime dot). BAGPIPES-sMILES returns significantly higher $\log_{10}(Z_*/Z_\odot)$, $[\text{Fe}/\text{H}]$ and $[\text{Mg}/\text{H}]$, and crucially no measurable t_{sq} value. This is caused by an extremely poorly constrained SFH for the BAGPIPES-sMILES fit, where the posterior median SFH rises gradually from $z > 10$ to $z \sim 5$, followed by a sharper decline to the time of observation. This broad, continuous SFH is in stark contrast to the results obtained in the fiducial fit and all other fitting configurations, suggesting that the limited wavelength baseline of the sMILES library, which greatly reduces the number of photometric bands that can be fitted, can seriously affect the accuracy and precision of quantities measured. In this case, assuming a simpler model such as a single burst in SFH can sufficiently reduce modelling complexity to return a more-accurate and better-constrained posterior estimate, as demonstrated by the $\alpha\text{lf-}\alpha\text{-sMILES}$ configuration (pink square).

From the left column of Fig. 8, it might appear that the BAGPIPES-sMILES fitting configuration (lime) shifts the stellar metallicity of 109760 and 113667, 2/3 of the metal-poor galaxies from our fiducial fits discussed in Section 3.3, up to approximately solar values, in line with the other galaxies. However, as discussed above, the BAGPIPES-sMILES results suffer from a reduced wavelength baseline, which leads to largely unconstrained SFHs. This affects both 109760 and 113667, hence their BAGPIPES-sMILES metallicity estimates are not trustworthy.

Whilst it is clear that our spectral fitting results with variable $[\alpha/\text{Fe}]$ abundances suffer from considerable systematics as discussed above, some sensible basic conclusions can be drawn. PRIMER-EXCELS-55410 (ZF-UDS-7329), an ultra-massive quiescent galaxy that assembled at $z \gtrsim 10$, exhibits the smallest uncertainties and the best agreement between the fitting configurations in all measured quantities shown in Fig. 8. This galaxy is likely solar or slightly super-solar in $[\alpha/\text{Fe}]$, which could indicate a moderately prolonged assembly time. This might be surprising when compared to this galaxy's measured SFH from our fiducial model, which suggests extremely early and relatively rapid assembly ($\tau_{10-90} \approx 300$ Myr, Fig. A1). However, the fiducial τ_{10-90} estimate is highly uncertain (≈ 250 Myr).

Despite their large uncertainties, the pair of ultra-massive quiescent galaxies at $z = 4.62$, 109760 and 117560 are consistent with stronger α -enhancement, with most fitting results for these objects favouring $[\text{Mg}/\text{Fe}] > 0.1$. This result is consistent with the extremely rapid formation and quenching required for the pair to be quiescent by only ≈ 1.3 Gyr after the Big Bang. One slightly lower

mass and lower redshift galaxy, 45981, appears to exhibit the weakest α -enhancement within the sample, as would be expected.

Lastly, it is worth noting that 113667 is one of the three objects discussed in Section 3 for which our fiducial [Bruzual & Charlot \(2003\)](#) fitting returns a very low stellar metallicity. This object displays the most severe disagreement between the different fitting runs in all measured quantities in Fig. 8, again suggesting that current stellar models are not well able to reproduce a subset of relatively young quiescent galaxies at $z > 3$.

4.2.2 Low-redshift MANGA control sample

As shown in the two lower rows in Fig. 8, better agreement is achieved between the five fitting configurations when fitting the local controls. We also observe a significant reduction in the uncertainties in $[\text{Mg}/\text{Fe}]$ compared to the high-redshift results, likely a result of the significantly higher SNR of the control spectra (SNR per $\text{\AA} > 500$).

Particularly good agreement is reached between the fitting configurations for the older “red and dead” MaNGA-11835-9101, while some disagreement remains when fitting the younger post-starburst MaNGA-12514-3702 (BPASS provides slightly more metal-poor results than the other fits). This again indicates that the SSP libraries achieve better mutual agreement at older stellar ages (e.g., [Jones et al. 2025](#)). Given the more-similar stellar age of MaNGA-12514-3702 to the younger high-redshift massive quiescent galaxies, the disagreements in the results from MaNGA-12514-3702 could be a reflection of the disagreements from our high-redshift sample, both caused by poorer consistency among SSP libraries at younger stellar ages.

4.3 Can we reliably measure the stellar chemical abundance patterns of the earliest quiescent galaxies?

In the previous section, we measured Fe and Mg abundances, total metallicities and α -enhancements (using $[\text{Mg}/\text{Fe}]$) for 6 massive quiescent galaxies in our sample, using three different α -varying SSP libraries, two different fitting codes and two different wavelength ranges. Despite only selecting the galaxies with moderately high SNR per $\text{\AA} > 6$ and older stellar ages (> 500 Myr), we observe substantial disagreements between the results from the different fitting configurations in all estimated properties for most galaxies. Disagreement in total metallicity, $[\text{Fe}/\text{H}]$ and $[\text{Mg}/\text{H}]$ can reach > 1 dex. Aside from the oldest and highest SNR galaxy, 55410, uncertainties in $[\text{Mg}/\text{Fe}]$ from most fitting configurations are > 0.15 dex, with the 1σ confidence interval in some cases spanning more than half of the prior space of $-0.2 < [\text{Mg}/\text{Fe}] < 0.6$. Although disagreement significantly decreases when fitting a local galaxy with much higher SNR per $\text{\AA} > 500$ and a much older stellar age, galaxies that recently quenched can still lead to considerable disagreement even in the very-high-SNR regime.

The sources of the disagreements and difficulties encountered when measuring chemical abundance patterns in high-redshift massive quiescent galaxies are fourfold:

- (i) Differences between predictions from different SSP libraries
- (ii) Differences between results from different wavelength ranges
- (iii) Different SFH models assumed in different codes
- (iv) Low continuum SNR in *JWST* high-redshift galaxy spectra

Firstly, there remains poor agreement between the different α -varying SSP libraries ([Byrne & Stanway 2023](#)). As seen in Fig. 8, $\log_{10}(Z_*/Z_\odot)$, $[\text{Fe}/\text{H}]$ and $[\text{Mg}/\text{H}]$ estimates obtained using BPASS are often much lower than the estimates from other fitting configurations and our fiducial [Bruzual & Charlot \(2003\)](#) results, particularly

when only fitting the `alf` wavelength range (blue dots). From testing several spectral libraries on a large sample of star clusters, Asa'd et al. (2025) found that theoretical spectral libraries tend to return lower stellar age and metallicity estimates, particularly when fitting low-SNR spectra, consistent with our findings for the theoretical BPASS library. We note that our comparison between α -varying SSP libraries would be made more complete, and this issue in particular could be more thoroughly addressed, by the inclusion of α -MC (Park et al. 2025), which is a new, fully theoretical SSP library computed from consistently α -enhanced isochrones and stellar spectral templates. However, the α -MC library is not yet publicly available.

Differences between α -abundance and Mg abundance could also contribute to the disagreement. Compared to other α -elements (e.g., Ca), the build-up of Mg is more strongly dominated by core-collapse supernovae (Kobayashi et al. 2020). Therefore, when a galaxy has super-solar (sub-solar) $[\alpha/\text{Fe}]$, the galaxy's $[\text{Mg}/\text{H}]$ and $[\text{Mg}/\text{Fe}]$ will be higher (lower) than its $[\alpha/\text{H}]$ and $[\alpha/\text{Fe}]$. This subtle difference could impact our results in Fig. 8, as we use slightly different approaches for evaluating the Mg abundances for different SSP libraries. We assume $[\text{Mg}/\text{H}] = [\alpha/\text{H}]$ and $[\text{Mg}/\text{Fe}] = [\alpha/\text{Fe}]$ for sMILES, convert α -abundances to Mg abundances when using BPASS, and report Mg abundances directly from the fits when using the Conroy et al. (2018) models. If we assume our sample generally have super-solar $[\alpha/\text{Fe}]$, this slight difference in approach between the SSP templates could partially explain the higher $[\text{Mg}/\text{Fe}]$ estimate for most of these objects returned by the BAGPIPES-BPASS-MILES-range fits (orange dots), compared to the BAGPIPES-sMILES fits (lime dots). It could also explain the higher $[\text{Mg}/\text{Fe}]$ estimate for 55410 and 117560 from `alf- α` using the Conroy et al. (2018) models (black squares), compared to using sMILES (magenta squares).

Secondly, galaxy properties measured by fitting different rest-frame wavelength ranges can lead to diverging results. This divergence varies with stellar age. Therefore, it is important to measure chemical abundances using a wide wavelength baseline to avoid being sensitive to only spectral features of one element, and to avoid only fitting spectral regions that are sensitive to limited stellar spectral types and stages of stellar evolution.

Thirdly, fits performed using `alf- α` assume a different SFH model (single burst) compared to those using BAGPIPES (double power-law). The increased flexibility from the extended SFH used in BAGPIPES could lead to estimates that diverge from ones made assuming all stars formed in a coeval burst (such as our fits for 109760, as discussed in Section 4.2). To test this, we repeated all BAGPIPES α -varying fits with single-burst SFH models. On average, when compared to their double-power-law counterparts, we found the measured $\log_{10}(Z_*/Z_\odot)$, $[\text{Mg}/\text{Fe}]$ and t_{form} differ by ≈ 0.3 dex, ≈ 0.12 dex and ≈ 0.15 Gyr, respectively. These magnitudes are comparable to some of the differences seen between `alf- α` and BAGPIPES estimates in Fig. 8 (e.g., comparing lime and magenta), thus the assumption of different SFH models plausibly contributes to the observed differences between results measured from the different fitting configurations described in Section 4.2.

Lastly, the SNRs of the *JWST* spectra obtained for these early massive quiescent galaxies remain too low, contributing to the large uncertainties and scatter in $[\text{Mg}/\text{Fe}]$ in Fig. 8. Although we observe the best agreements between the fitting configurations in 55410, the level of precision achieved allows relatively little to be concluded beyond that it likely has a solar or slightly super-solar α -abundance ratio. Therefore, we estimate the minimum SNR per \AA required for useful α -abundance measurements to be $\gtrsim 15$, slightly above that of our 55410 observation (which has SNR per $\text{\AA} \simeq 12$).

In summary, when measuring detailed chemical abundances and

α -enhancement, it is desirable to always report results from more than one fitting configuration, ideally using various SSP libraries. A wide wavelength baseline should be used, and a minimal SNR per $\text{\AA} \gtrsim 15$ is needed. This corresponds to a SNR per resolution element of $\gtrsim 100$ for medium-resolution ($R \simeq 1000$) spectroscopy.

4.3.1 α -abundance in PRIMER-UDS-55410 (ZF-UDS-7329)

In Fig. 8, using `alf- α` with the Conroy et al. (2018) models, we estimate that the most massive galaxy in our sample, 55410 (ZF-UDS-7329), has $[\text{Mg}/\text{Fe}] = 0.08^{+0.11}_{-0.12}$. This is in tension at a $\simeq 1.7\sigma$ level with the measurement of $[\text{Mg}/\text{Fe}] = 0.42^{+0.19}_{-0.17}$ for this object using `alf` by Carnall et al. (2024).

To investigate the source of this disagreement, we produced an alternative spectrum for 55410 using the same level 3 output 2D spectra produced in Section 2.2.1, but following the method of Carnall et al. (2024) when performing 1D optimal extraction, joining of the three gratings and spectrophotometric calibration. The only differences therefore between this spectrum and the one analysed by Carnall et al. (2024) should be due to updates in the *JWST* pipeline and calibration reference files (Carnall et al. 2024 used v1.12.5 of the *JWST* pipeline and CRDS_CTX=jwst_1183.pmap, compared to our pipeline v1.19.1 and CRDS_CTX=jwst_1413.pmap).

Fitting this new spectrum using `alf- α` and the Conroy et al. (2018) models yields $[\text{Mg}/\text{Fe}] = 0.09^{+0.11}_{-0.12}$, which is consistent with the result in Fig. 8 using the same code and model configuration, but again different to the Carnall et al. (2024) result. This rejects the updates we have made to our 1D optimal extraction, grating joining and spectrophotometric calibration procedures as the cause of the disagreement with Carnall et al. (2024). We also fit the spectrum used in Carnall et al. (2024) with `alf- α` and the Conroy et al. (2018) models, yielding $[\text{Mg}/\text{Fe}] = 0.29 \pm 0.12$, which is more consistent with the value given by `alf` in Carnall et al. (2024). This suggests the switch from `alf` to `alf- α` only introduced a minor difference. We thus conclude that the disagreement is largely due to changes in the NIRSpec reduction pipeline and calibration reference files since early 2024.

4.4 Impact on stellar age and total metallicity estimates

We finally discuss the impact that fitting α -enhancement as a free parameter can have on estimates for stellar age and total metallicity, which could influence the conclusions we have drawn in Section 3. As discussed in Section 3.3, Beverage et al. (2025) have reported that assuming scaled-solar abundances can produce up to $\simeq 0.8 - 0.9$ dex biases in total stellar metallicities, compared to methods that measure individual chemical abundances. Here, we expand the investigation of this issue to our wider variety of code, model and wavelength-range configurations.

In Fig. 9, we plot the difference between the t_{form} and $\log_{10}(Z_*/Z_\odot)$ estimates returned by each α -varying fitting configuration and the fiducial results from the BC03 fits. Several fitting results with outlying Δt_{form} and/or $\Delta \log_{10}(Z_*/Z_\odot)$ values can be clearly seen, namely BAGPIPES-BPASS-`alf` range for 45981, 50789, 113667 and 117560, and BAGPIPES-sMILES for 109760. These fits have already been determined as obviously problematic above in Section 4.2.1. Once the outliers are removed, the top panel of Fig. 9 shows that offsets in t_{form} do not exceed 0.5 Gyr when alpha abundance is varied.

We measure the typical Δt_{form} between α -enhanced and non- α -enhanced runs by measuring the standard deviation via the median

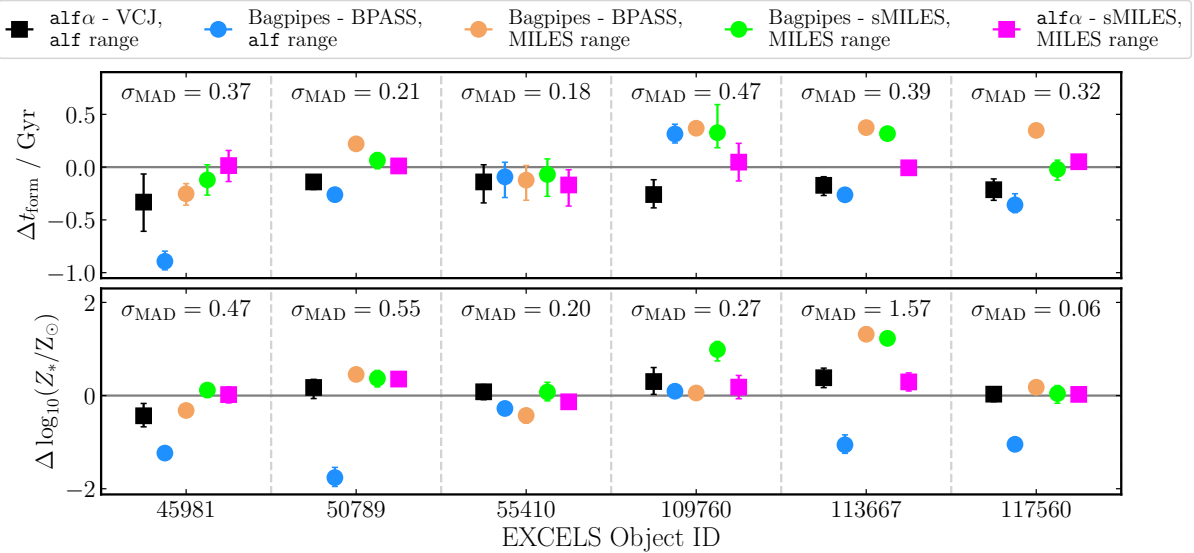


Figure 9. Differences in estimated galaxy physical properties between our fiducial [Bruzual & Charlot \(2003\)](#) run and our 5 fitting configurations with variation in α -abundances for the same 6 massive quiescent galaxies shown in Fig. 8. The top row shows the age of the Universe when 50 per cent of galaxy stellar mass had formed (t_{form}) and the bottom row shows stellar metallicity. Positive values indicate that the α -varying estimate is higher than the fiducial result. In each panel, we also include the standard deviation (estimated via the median absolute deviation) of the differences in both properties for each galaxy, calculated across the 5 configurations. The colours again follow the scheme given in Fig. 8 and Table 3.

absolute deviation across all configurations in all galaxies, obtaining $\sigma_{\text{MAD}} = 0.29$ Gyr. This is considerably smaller than the range spanned by our sample (Fig. 5). Thus, the lack of α -variation in our fiducial fits does not strongly affect our conclusions in Sections 3 and 3.2.2 concerning downsizing.

Similarly, once outlying results are removed from the lower panel of Fig. 9, $\log_{10}(Z_*/Z_\odot)$ estimates from the fiducial fit have offsets not exceeding 0.7 dex. This is slightly smaller than, but in generally good agreement with, the maximum offsets of $\simeq 0.8 - 0.9$ dex observed by [Beverage et al. \(2025\)](#). We measure $\sigma_{\text{MAD}} = 0.4$ dex, again comparable with the $\simeq 0.3$ dex scatter reported by [Beverage et al. \(2025\)](#). Lastly, [Beverage et al. \(2025\)](#) reported that $\log_{10}(Z_*/Z_\odot)$ measured when varying α -enhancement are offset by $\sim +0.4$ dex compared to non- α -enhanced measurements. We do not observe such an offset in our results from Fig. 9.

5 CONCLUSIONS

We have investigated the evolution and quenching of massive galaxies in the first 2 billion years of cosmic time with a sample of 14 massive quiescent galaxies at $3 < z < 5$ benefiting from extremely deep, medium-resolution ($R \simeq 1000$) continuum spectroscopy at $\lambda = 1 - 5 \mu\text{m}$ from the *JWST* EXCELS survey. We perform a full, customised re-reduction of the EXCELS spectroscopy, introducing a novel wavelength-varying 1D optimal extraction method that combats the spectral “wiggles” caused by undersampling of the NIRSpec point spread function in the cross-dispersion (spatial) direction (see Section 2.2.2). This reduces the amplitude of the “wiggles” from $\simeq 5$ per cent to $\simeq 1$ per cent in the most problematic cases.

We analyse the spectroscopic data, along with the available multi-wavelength *HST*+*JWST* photometry, using Bayesian full spectra fitting, producing our main set of fiducial results with the [Bruzual & Charlot \(2003\)](#) stellar population models. We obtain good constraints for 12 galaxies with the other 2 objects having insufficient SNR.

We find that massive quiescent galaxies at $3 < z < 5$ exhibit a tight negative correlation between their stellar mass and formation time (see Fig. 5), indicating that more massive galaxies assembled the bulk of their stellar mass earlier than less massive ones. Thus, the “downsizing” trend well known at lower redshift was already in place by $z \sim 4$. We fit the slope of the stellar mass-formation time relation, finding that it is consistent with those derived from various samples of spectroscopically observed massive quiescent galaxies at $0 < z < 3$ from the literature (see Fig. 6), at $\simeq 1.5$ Gyr per decade in stellar mass (Equation 1). It is particularly noteworthy that we do not find any lower-mass relic galaxies in our sample: no objects with $\log_{10}(M_*/M_\odot) < 10.8$ have formation times earlier than $\simeq 1$ Gyr after the Big Bang. Therefore we conclude that $\log_{10}(M_*/M_\odot) \simeq 10$ quiescent galaxies at higher redshift, such as the $z = 7.3$ quiescent galaxy recently reported in [Weibel et al. \(2025\)](#), will likely rejuvenate on timescales of a few hundred Myr.

The fitted SFHs suggest that most early massive quiescent galaxies experienced extremely rapid assembly of their stellar mass, forming 80 per cent of their stellar mass in only ~ 200 Myr. Their high peak SFRs ($> 300 M_\odot \text{ yr}^{-1}$) are comparable to the SFRs of the most extreme submillimetre galaxies at higher redshifts ($z \gtrsim 5$).

The majority of our sample have relatively high stellar metallicities, comparable with results for literature massive quiescent galaxies from $0 < z < 3$ (see Figs 5 and 6), though we find no clear stellar mass-metallicity relation from our relatively small sample. Three objects however are fitted as much more metal poor, at $\log_{10}(Z_*/Z_\odot) \approx -0.8$. This has also been reported for some of the other highest redshift massive quiescent galaxies in the literature ([Carnall et al. 2023b; de Graaff et al. 2025; Wu 2025; Weibel et al. 2025](#)), potentially indicating a new evolutionary pathway for massive, early galaxies that rapidly formed and quenched whilst maintaining substantially sub-solar metallicities. However, as no such objects are found at lower redshift, we caution that it is also highly plausible that these results are due to an inadequacy of current stellar models in the relatively little explored $\simeq 500$ Myr age range that many $3 < z < 5$

massive quiescent galaxies inhabit. We test fitting these objects whilst imposing higher stellar metallicities, finding no significant impact on our derived stellar mass-formation time relationship.

Next, and partly motivated by these results, we investigate the detailed stellar chemical abundances of our sample, in particular their α -enhancements, which we measure as $[\text{Mg}/\text{Fe}]$ (our fiducial [Bruzual & Charlot 2003](#) fits assume scaled-solar abundances). For a sub-sample of the oldest 6 galaxies with higher SNR, we have tested 5 fitting configurations with varying combinations of fitting code, α -abundance-varying SSP library, and fitted wavelength range (see Section 4.1 and Table 3). We find considerable disagreement between the total metallicities and abundance ratios measured by the 5 fitting configurations (see Section 4.2 and Fig. 8). These differences are contributed to by deviations between the predictions of different SSP libraries, by differing fitted wavelength ranges, different assumed SFH models, and the limited wavelength baseline of some SSP libraries, as well as showing some evidence of being exacerbated by younger galaxy stellar ages (see Section 4.3).

We observe large uncertainties in most of our estimated $[\text{Mg}/\text{Fe}]$ abundance ratios, suggesting that spectra with higher SNR than is typical for our sample are required for robust measurements of α -enhancement. We suggest that future high-redshift studies should aim for observed-frame SNR per $\text{\AA} \gtrsim 15$ over $5100 < \lambda_{\text{rest}} < 6400 \text{\AA}$. Despite these challenges, from comparing the α -varying results with our fiducial scaled-solar abundance results using [Bruzual & Charlot \(2003\)](#), we find that the assumption of the solar abundance mixture (scaled-solar abundances) likely introduces only fairly limited biases into our fiducial estimates of galaxy formation times (t_{form}) and total stellar metallicity (see Section 4.4 and Fig. 9).

Measuring detailed stellar chemical abundances for the earliest quiescent galaxies therefore remains highly challenging. The models that such measurements rely on (SSP libraries including variable non-solar abundance mixtures) are still in the early stages of development. We therefore suggest that future observational works aiming to measure detailed stellar elemental abundances should report estimates from more than one model library fitted to a wide wavelength baseline, thus mitigating (or at least exposing) potential biases caused by only using one fitting configuration. Considerably higher-SNR continuum spectra for the earliest quiescent galaxies at $3 < z < 5$ will also be needed to obtain precise measurements of their detailed chemical abundances. Current medium-resolution data from surveys such as EXCELS are however sufficient to measure the stellar ages of such systems, and to provide a first indication of their total stellar metallicities, allowing us to begin moving towards understanding how stellar mass assembly and the quenching of star formation took place in the early Universe.

ACKNOWLEDGEMENTS

We thank Yingjie Peng for providing data. HL thanks Anne Sansom and Elizabeth Stanway for discussions that helped with interpreting α -enhancement results. HL, ACC, ET and SDS acknowledge support from a UKRI Frontier Research Grantee Grant (PI Carnall; grant reference EP/Y037065/1). FC, KZA-C, DS and TMS acknowledge support from a UKRI Frontier Research Guarantee Grant (PI Cullen; grant reference EP/X021025/1). VW acknowledges Science and Technologies Facilities Council (STFC) grants ST/V000861/1 and ST/Y00275X/1, and Leverhulme Research Fellowship RF-2024-589/4. OA acknowledges the support from STFC grant ST/X006581/1. JSD and DJM acknowledge the support of the Royal Society through the award of a Royal Society University

Research Professorship to JSD. Support for Program number JWST-GO-03543.014 was provided through a grant from the STScI under NASA contract NAS5-03127.

Software: ASTROPY ([Astropy Collaboration et al. 2013](#)), BAGPIPES ([Carnall et al. 2018, 2019a](#)), CELERITE2 ([Foreman-Mackey et al. 2017; Foreman-Mackey 2018](#)), MARVIN ([Cherinka et al. 2019](#)), MATPLOTLIB ([Hunter 2007](#)), NAUTILUS ([Lange 2023b](#)), NUMBA ([Lam et al. 2015](#)), NUMPY ([Harris et al. 2020](#)), PIPES_VIS ([Leung et al. 2021](#)), SCIPY ([Virtanen et al. 2020](#)), SEABORN ([Waskom 2021](#))

For the purpose of open access, the author has applied a Creative Commons Attribution (CC BY) licence to any Author Accepted Manuscript version arising from this submission.

DATA AVAILABILITY

All JWST and HST data used in this work are available via the Mikulski Archive for Space Telescopes (<https://mast.stsci.edu>). The reduced, extracted, calibrated and joined 1D spectra for all 14 galaxies, along with a machine readable version of Table 2 is available at [url1](#). Additional data products are available from the authors upon request.

REFERENCES

Abramson L. E., Gladders M. D., Dressler A., Oemler Jr. A., Poggianti B., Vulcani B., 2016, *ApJ*, **832**, 7
 Alberts S., et al., 2024, *ApJ*, **975**, 85
 Antwi-Danso J., et al., 2025, *ApJ*, **978**, 90
 Asa'd R., Coelho P. R. T., John J. M., Chilingarian I. V., Bruzual G., Charlot S., 2025, *AJ*, **170**, 85
 Asplund M., Grevesse N., Sauval A. J., 2005, in Barnes III T. G., Bash F. N., eds, *Astronomical Society of the Pacific Conference Series* Vol. 336, *Cosmic Abundances as Records of Stellar Evolution and Nucleosynthesis*, p. 25
 Asplund M., Grevesse N., Sauval A. J., Scott P., 2009, *ARA&A*, **47**, 481
 Astropy Collaboration et al., 2013, *A&A*, **558**, A33
 Baggen J. F. W., et al., 2023, *ApJ*, **955**, L12
 Baker W. M., et al., 2025a, *MNRAS*, **539**, 557
 Baker W. M., et al., 2025b, *A&A*, **702**, A270
 Baldwin J. A., Phillips M. M., Terlevich R., 1981, *PASP*, **93**, 5
 Baldwin C., McDermid R. M., Kuntschner H., Maraston C., Conroy C., 2018, *MNRAS*, **473**, 4698
 Barrufet L., et al., 2025, *MNRAS*, **537**, 3453
 Begley R., et al., 2025, *MNRAS*, **537**, 3245
 Behroozi P. S., Conroy C., Wechsler R. H., 2010, *ApJ*, **717**, 379
 Belli S., Newman A. B., Ellis R. S., 2019, *ApJ*, **874**, 17
 Belli S., et al., 2024, *Nature*, **630**, 54
 Bertin E., Arnouts S., 1996, *A&AS*, **117**, 393
 Beverage A. G., Kriek M., Conroy C., Bezanson R., Franx M., van der Wel A., 2021, *ApJ*, **917**, L1
 Beverage A. G., Kriek M., Conroy C., Sandford N. R., Bezanson R., Franx M., van der Wel A., Weisz D. R., 2023, *ApJ*, **948**, 140
 Beverage A. G., et al., 2024, *ApJ*, **966**, 234
 Beverage A. G., et al., 2025, *ApJ*, **979**, 249
 Bing L., et al., 2025, *arXiv e-prints*, p. arXiv:2511.08672
 Bruzual G., Charlot S., 2003, *MNRAS*, **344**, 1000
 Bugiani L., et al., 2025, *ApJ*, **981**, 25
 Bundy K., et al., 2015, *ApJ*, **798**, 7
 Bushouse H., et al., 2025, JWST Calibration Pipeline, [doi:10.5281/zenodo.6984365](https://doi.org/10.5281/zenodo.6984365)
 Byler N., Dalcanton J. J., Conroy C., Johnson B. D., 2017, *ApJ*, **840**, 44
 Byrne C. M., Stanway E. R., 2023, *MNRAS*, **521**, 4995
 Byrne C. M., Stanway E. R., Eldridge J. J., McSwiney L., Townsend O. T., 2022, *MNRAS*, **512**, 5329

Byrne C. M., Eldridge J. J., Stanway E. R., 2025, *MNRAS*, **537**, 2433

Calzetti D., Armus L., Bohlin R. C., Kinney A. L., Koornneef J., Storchi-Bergmann T., 2000, *ApJ*, **533**, 682

Cappellari M., 2017, *MNRAS*, **466**, 798

Caputi K. I., Dunlop J. S., McLure R. J., Roche N. D., 2004, *MNRAS*, **353**, 30

Carnall A. C., 2017, preprint, ([arXiv:1705.05165](https://arxiv.org/abs/1705.05165))

Carnall A. C., McLure R. J., Dunlop J. S., Davé R., 2018, *MNRAS*, **480**, 4379

Carnall A. C., et al., 2019a, *MNRAS*, **490**, 417

Carnall A. C., Leja J., Johnson B. D., McLure R. J., Dunlop J. S., Conroy C., 2019b, *ApJ*, **873**, 44

Carnall A. C., et al., 2020, *MNRAS*, **496**, 695

Carnall A. C., et al., 2022, *ApJ*, **929**, 131

Carnall A. C., et al., 2023a, *MNRAS*, **520**, 3974

Carnall A. C., et al., 2023b, *Nature*, **619**, 716

Carnall A. C., et al., 2024, *MNRAS*, **534**, 325

Cattaneo A., Dekel A., Faber S. M., Guiderdoni B., 2008, *MNRAS*, **389**, 567

Chaikin E., et al., 2025, *arXiv e-prints*, p. [arXiv:2509.04067](https://arxiv.org/abs/2509.04067)

Chandro-Gómez Á., et al., 2025, *arXiv e-prints*, p. [arXiv:2512.16208](https://arxiv.org/abs/2512.16208)

Chehade B., et al., 2018, *MNRAS*, **478**, 1649

Cheng C. M., et al., 2024, *MNRAS*, **532**, 3604

Cherinka B., et al., 2019, *AJ*, **158**, 74

Chevallard J., Charlot S., 2016, *MNRAS*, **462**, 1415

Choi J., Conroy C., Johnson B. D., 2019, *ApJ*, **872**, 136

Cid Fernandes R., Stasińska G., Mateus A., Vale Asari N., 2011, *MNRAS*, **413**, 1687

Cimatti A., et al., 2004, *Nature*, **430**, 184

Conroy C., 2013, *Annual Review of Astronomy and Astrophysics*, **51**, 393

Conroy C., Gunn J. E., 2010, *ApJ*, **712**, 833

Conroy C., van Dokkum P. G., 2012, *ApJ*, **760**, 71

Conroy C., Graves G. J., van Dokkum P. G., 2014, *ApJ*, **780**, 33

Conroy C., Villaume A., van Dokkum P. G., Lind K., 2018, *ApJ*, **854**, 139

Cowie L. L., Songaila A., Hu E. M., Cohen J. G., 1996, *AJ*, **112**, 839

Croton D. J., et al., 2006, *MNRAS*, **365**, 11

Cullen F., et al., 2021, *MNRAS*, **505**, 903

Daddi E., et al., 2005, *ApJ*, **626**, 680

Davies R. L., et al., 2024, *MNRAS*, **528**, 4976

Dekel A., Birnboim Y., 2006, *MNRAS*, **368**, 2

Dekel A., Sarkar K. C., Birnboim Y., Mandelker N., Li Z., 2023, *MNRAS*, **523**, 3201

Dekel A., Mandelker N., Li Z., Yao Z., Zhu B., Lapiner S., Dutta Chowdhury D., Ginzburg O., 2025, *MNRAS*, **544**, 160

Dumont A., et al., 2025, *A&A*, **703**, A54

Dunlop J., Peacock J., Spinrad H., Dey A., Jimenez R., Stern D., Windhorst R., 1996, *Nature*, **381**, 581

Dunlop J. S., et al., 2021, PRIMER: Public Release IMaging for Extragalactic Research, JWST Proposal. Cycle 1, ID. #1837

Estrada-Carpenter V., et al., 2019, *ApJ*, **870**, 133

Falcón-Barroso J., Sánchez-Blázquez P., Vazdekis A., Ricciardelli E., Cardiel N., Cenarro A. J., Gorgas J., Peletier R. F., 2011, *A&A*, **532**, A95

Ferland G. J., et al., 2017, *Rev. Mex. Astron. Astrofis.*, **53**, 385

Ferré-Mateu A., Trujillo I., Martín-Navarro I., Vazdekis A., Mezcua M., Balcells M., Domínguez L., 2017, *MNRAS*, **467**, 1929

Fontana A., et al., 2009, *A&A*, **501**, 15

Foreman-Mackey D., 2018, *Research Notes of the American Astronomical Society*, **2**, 31

Foreman-Mackey D., Agol E., Ambikasaran S., Angus R., 2017, *AJ*, **154**, 220

Forrest B., et al., 2020a, *ApJ*, **890**, L1

Forrest B., et al., 2020b, *ApJ*, **903**, 47

Fruchter A. S., Hook R. N., 2002, *PASP*, **114**, 144

Gallazzi A., Charlot S., Brinchmann J., White S. D. M., Tremonti C. A., 2005, *MNRAS*, **362**, 41

Gallazzi A., Bell E. F., Zibetti S., Brinchmann J., Kelson D. D., 2014, *ApJ*, **788**, 72

Glazebrook K., et al., 2017, *Nature*, **544**, 71

Glazebrook K., et al., 2024, *Nature*, **628**, 277

Greene J. E., Ho L. C., 2005, *ApJ*, **630**, 122

Grogan N. A., et al., 2011, *The Astrophysical Journal Supplement Series*, **197**, 35

Hamadouche M. L., et al., 2023, *MNRAS*, **521**, 5400

Harris C. R., et al., 2020, *Nature*, **585**, 357

Hartley A. I., et al., 2023, *MNRAS*, **522**, 3138

Hogg D. W., Bovy J., Lang D., 2010, preprint, ([arXiv:1008.4686](https://arxiv.org/abs/1008.4686))

Horne K., 1986, *PASP*, **98**, 609

Hunt L. K., et al., 2019, *A&A*, **621**, A51

Hunter J. D., 2007, *Computing in Science and Engineering*, **9**, 90

Illingworth G., et al., 2016, *arXiv e-prints*, p. [arXiv:1606.00841](https://arxiv.org/abs/1606.00841)

Inoue A. K., Shimizu I., Iwata I., Tanaka M., 2014, *MNRAS*, **442**, 1805

Ito K., et al., 2025, *A&A*, **697**, A111

Jafariyazani M., Newman A. B., Mobasher B., Belli S., Ellis R. S., Patel S. G., 2020, *ApJ*, **897**, L42

Jafariyazani M., Newman A. B., Mobasher B., Belli S., Ellis R. S., Faisst A. L., 2025, *ApJ*, **986**, 148

Jin S., et al., 2024, *A&A*, **683**, L4

Jones G. T., Byrne C. M., Stanway E. R., 2025, *MNRAS*, **543**, 167

Kimmig L. C., Remus R.-S., Seidel B., Valenzuela L. M., Dolag K., Burkert A., 2025, *ApJ*, **979**, 15

Knowles A. T., Sansom A. E., Allende Prieto C., Vazdekis A., 2021, *MNRAS*, **504**, 2286

Knowles A. T., Sansom A. E., Vazdekis A., Allende Prieto C., 2023, *MNRAS*, **523**, 3450

Kobayashi C., Karakas A. I., Lugaro M., 2020, *ApJ*, **900**, 179

Koekemoer A. M., et al., 2011, *The Astrophysical Journal Supplement Series*, **197**, 36

Kormendy J., Ho L. C., 2013, *ARA&A*, **51**, 511

Kriek M., et al., 2016, *Nature*, **540**, 248

Kriek M., et al., 2019, *ApJ*, **880**, L31

Kriek M., et al., 2024, *ApJ*, **966**, 36

Krishna S. D., Wild V., Hewett P. C., Villforth C., 2025, *MNRAS*, **543**, 1535

Kron R. G., 1980, *ApJS*, **43**, 305

Kroupa P., 2001, *MNRAS*, **322**, 231

Lagos C. d. P., et al., 2025, *MNRAS*, **536**, 2324

Lam S. K., Pitrou A., Seibert S., 2015, in *Proceedings of the Second Workshop on the LLVM Compiler Infrastructure in HPC*. pp 1–6

Lange J. U., 2023a, *MNRAS*, **525**, 3181

Lange J. U., 2023b, *Monthly Notices of the Royal Astronomical Society*, **525**, 3181

Leja J., Carnall A. C., Johnson B. D., Conroy C., Speagle J. S., 2019, *ApJ*, **876**, 3

Leja J., et al., 2022, *ApJ*, **936**, 165

Leung H.-H., Wild V., Carnall A., Papathomas M., 2021, *Research Notes of the American Astronomical Society*, **5**, 171

Leung H.-H., Wild V., Papathomas M., Carnall A., Zheng Y., Boardman N., Wang C., Johansson P. H., 2024, *MNRAS*, **528**, 4029

Leung H.-H., Wild V., Papathomas M., Carnall A. C., Chen Y., 2025, *MNRAS*, **543**, 738

Liu F.-Y., et al., 2025, *MNRAS*,

Long A. S., et al., 2024, *ApJ*, **970**, 68

Lonoce I., et al., 2015, *MNRAS*, **454**, 3912

Lovell C. C., et al., 2023, *MNRAS*, **525**, 5520

Maiolino R., Mannucci F., 2019, *A&ARv*, **27**, 3

Maiolino R., et al., 2024, *A&A*, **691**, A145

Man A. W. S., et al., 2021, *ApJ*, **919**, 20

Maoz D., Mannucci F., Brandt T. D., 2012, *MNRAS*, **426**, 3282

Maseda M. V., et al., 2023, *ApJ*, **956**, 11

McLeod D. J., et al., 2024, *MNRAS*, **527**, 5004

McLure R. J., Jarvis M. J., Targett T. A., Dunlop J. S., Best P. N., 2006, *MNRAS*, **368**, 1395

McLure R. J., et al., 2018, *MNRAS*, **479**, 25

Merlin E., et al., 2018, *MNRAS*, **473**, 2098

Merlin E., et al., 2019, *MNRAS*, **490**, 3309

Merlin E., et al., 2025, *The Open Journal of Astrophysics*, **8**, E170

Michałowski M. J., et al., 2017, *MNRAS*, **469**, 492

Moster B. P., Naab T., White S. D. M., 2018, *MNRAS*, **477**, 1822

Murga M., Zhu G., Ménard B., Lan T.-W., 2015, *MNRAS*, **452**, 511

Nanayakkara T., et al., 2024, *Scientific Reports*, **14**, 3724

Nelson D., et al., 2018, *MNRAS*, **475**, 624

Ocvirk P., Pichon C., Lançon A., Thiébaut E., 2006, *MNRAS*, **365**, 46

Oke J. B., Gunn J. E., 1983, *ApJ*, **266**, 713

Onodera M., et al., 2015, *ApJ*, **808**, 161

Onoue M., et al., 2019, *ApJ*, **880**, 77

Pacifci C., Charlot S., Blaizot J., Brinchmann J., 2012, *MNRAS*, **421**, 2002

Pacucci F., Loeb A., 2024, *ApJ*, **964**, 154

Panter B., Jimenez R., Heavens A. F., Charlot S., 2008, *MNRAS*, **391**, 1117

Park M., et al., 2024, *ApJ*, **976**, 72

Park M., Conroy C., Johnson B. D., Leja J., Dotter A., Cargile P. A., 2025, *ApJ*, **994**, 165

Peng Y., Maiolino R., Cochrane R., 2015, *Nature*, **521**, 192

Pentericci L., et al., 2018, *A&A*, **616**, A174

Pérez-González P. G., et al., 2008, *ApJ*, **675**, 234

Perna M., et al., 2023, *A&A*, **679**, A89

Pforr J., Maraston C., Tonini C., 2012, *MNRAS*, **422**, 3285

Popesso P., et al., 2023, *MNRAS*, **519**, 1526

Remus R.-S., Kimmig L. C., 2025, *ApJ*, **982**, 30

Rennehan D., 2024, *ApJ*, **975**, 114

Rodríguez-Puebla A., Primack J. R., Avila-Reese V., Faber S. M., 2017, *MNRAS*, **470**, 651

Russell T. A., et al., 2025, *MNRAS*,

Salim S., Boquien M., Lee J. C., 2018, *ApJ*, **859**, 11

Sánchez-Blázquez P., et al., 2006, *MNRAS*, **371**, 703

Scannapieco E., Silk J., Bouwens R., 2005, *ApJ*, **635**, L13

Schaye J., et al., 2025, *arXiv e-prints*, p. arXiv:2508.21126

Schreiber C., et al., 2018, *A&A*, **618**, A85

Setton D. J., et al., 2024, *ApJ*, **974**, 145

Shapley A. E., et al., 2025, *ApJ*, **980**, 242

Silk J., Begelman M. C., Norman C., Nusser A., Wyse R. F. G., 2024, *ApJ*, **961**, L39

Skarbinski M., et al., 2025, *arXiv e-prints*, p. arXiv:2509.18278

Slob M., et al., 2024, *ApJ*, **973**, 131

Slob M., et al., 2025, *A&A*, **702**, A110

Speagle J. S., Steinhardt C. L., Capak P. L., Silverman J. D., 2014, *ApJS*, **214**, 15

Spinello C., et al., 2021, *A&A*, **646**, A28

Stanton T. M., et al., 2024, *MNRAS*, **532**, 3102

Steidel C. C., Strom A. L., Pettini M., Rudie G. C., Reddy N. A., Trainor R. F., 2016, *ApJ*, **826**, 159

Stevenson S. D., et al., 2025, *MNRAS*,

Straatman C. M. S., et al., 2014, *ApJ*, **783**, L14

Straatman C. M. S., et al., 2016, *ApJ*, **830**, 51

Taylor E., Almaini O., Merrifield M., Maltby D., Wild V., Hartley W. G., Rowlands K., 2023, *MNRAS*, **522**, 2297

Taylor E., et al., 2026, *arXiv e-prints*, p. arXiv:2601.02269

Thomas D., Maraston C., Bender R., 2003, *MNRAS*, **339**, 897

Thomas D., Maraston C., Bender R., Mendes de Oliveira C., 2005, *ApJ*, **621**, 673

Thomas D., Maraston C., Schawinski K., Sarzi M., Silk J., 2010, *MNRAS*, **404**, 1775

Topping M. W., Shapley A. E., Reddy N. A., Sanders R. L., Coil A. L., Kriek M., Mobasher B., Siana B., 2020, *MNRAS*, **499**, 1652

Trussler J., Maiolino R., Maraston C., Peng Y., Thomas D., Goddard D., Lian J., 2020, *MNRAS*, **491**, 5406

Urbano Stawinski S. M., et al., 2024, *The Open Journal of Astrophysics*, **7**, 46

Valentino F., et al., 2020, *ApJ*, **889**, 93

Valentino F., et al., 2023, *ApJ*, **947**, 20

Vanden Berk D. E., et al., 2001, *AJ*, **122**, 549

Vazdekis A., et al., 2015, *MNRAS*, **449**, 1177

Virtanen P., et al., 2020, *Nature Methods*, **17**, 261

Waskom M. L., 2021, *Journal of Open Source Software*, **6**, 3021

Weibel A., et al., 2025, *ApJ*, **983**, 11

Weller E. J., Pacucci F., Ni Y., Hernquist L., Park M., 2025, *ApJ*, **979**, 181

Whitaker K. E., et al., 2019, *ApJS*, **244**, 16

Wild V., et al., 2020, *MNRAS*, **494**, 529

Table B1. Solar metal abundances from two commonly used solar chemical composition studies. The individual elemental abundances are given in the form $12 + \log_{10}(N_X/N_H)$ where X is the element. Here, we denote this form as A_X .

Paper	Proto-solar Z	Photosphere Z	$A_{\text{Fe},\odot}$	$A_{\text{Mg},\odot}$
Asplund et al. (2005)	0.0130	0.0122	7.45 ± 0.05	7.53 ± 0.09
Asplund et al. (2009)	0.0142	0.0134	7.50 ± 0.04	7.60 ± 0.04

Worley G., 1994, *ApJS*, **95**, 107

Wu P.-F., 2025, *ApJ*, **978**, 131

Zhuang Z., et al., 2023, *ApJ*, **948**, 132

de Graaff A., et al., 2025, *Nature Astronomy*, **9**, 280

van der Wel A., et al., 2016, *ApJS*, **223**, 29

APPENDIX A: STAR-FORMATION HISTORIES

Fig. A1 shows the fitted SFHs of the 12 massive quiescent galaxies for which we obtain good constraints from the BAGPIPES full-spectra-fitting approach described in 2.3. The 2 galaxies with low SNR and missing coverage around $\lambda_{\text{rest}} \sim 4000 \text{ \AA}$ are not shown.

APPENDIX B: CHEMICAL ABUNDANCE SCALE CONVERSIONS

Various SSP libraries often assume different solar metallicity scales and abundance mixtures. To compare results across these libraries properly, these values must first be converted into a common scale. For this work, we choose the solar metallicity scale and abundance mixture from Asplund et al. (2009). For Fig. 8 we require the abundance ratios $[\text{Fe}/\text{H}]$, $[\text{Mg}/\text{H}]$ and $[\text{Mg}/\text{Fe}]$, while the BAGPIPES fitting methodologies described in Section 4.1 only directly measure $\log_{10}(Z_*/Z_{\odot})$ and $[\alpha/\text{Fe}]$. Additional conversion is thus needed. Appendix B1 details the conversion for BPASS v2.3, while Appendix B2 details the conversion for sMILES. The Conroy et al. (2018) models are already on the Asplund et al. (2009) scale, and $\text{alf-}\alpha$ directly provides all abundance ratios plotted in Fig. 8, so no conversions are required.

In Table B1, we list the solar abundance values from two studies relevant in the rest of this section. For this section, we denote the expression $12 + \log_{10}(N_X/N_H)$ as A_X , where N_X and N_H are the number of atoms of the element in concern and Hydrogen per unit volume, respectively.

B1 The BPASS library

BPASS v2.3 provides an abundance table in their public release⁴. For each SSP, this table lists its metallicity (in mass fraction form), $[\alpha/\text{Fe}]$, and the abundances of several key elements in the form A_X . This includes values for H, Fe and Mg. $[\alpha/\text{Fe}]$ is given calibrated to the Asplund et al. (2009) abundance scale.

Therefore, to perform the conversion from given $\log_{10}(Z_*/Z_{\odot})$

⁴ Found in abundances_2024.zip in <https://warwick.ac.uk/fac/sci/physics/research/astro/research/catalogues/bpass/bpassv2p3/>.

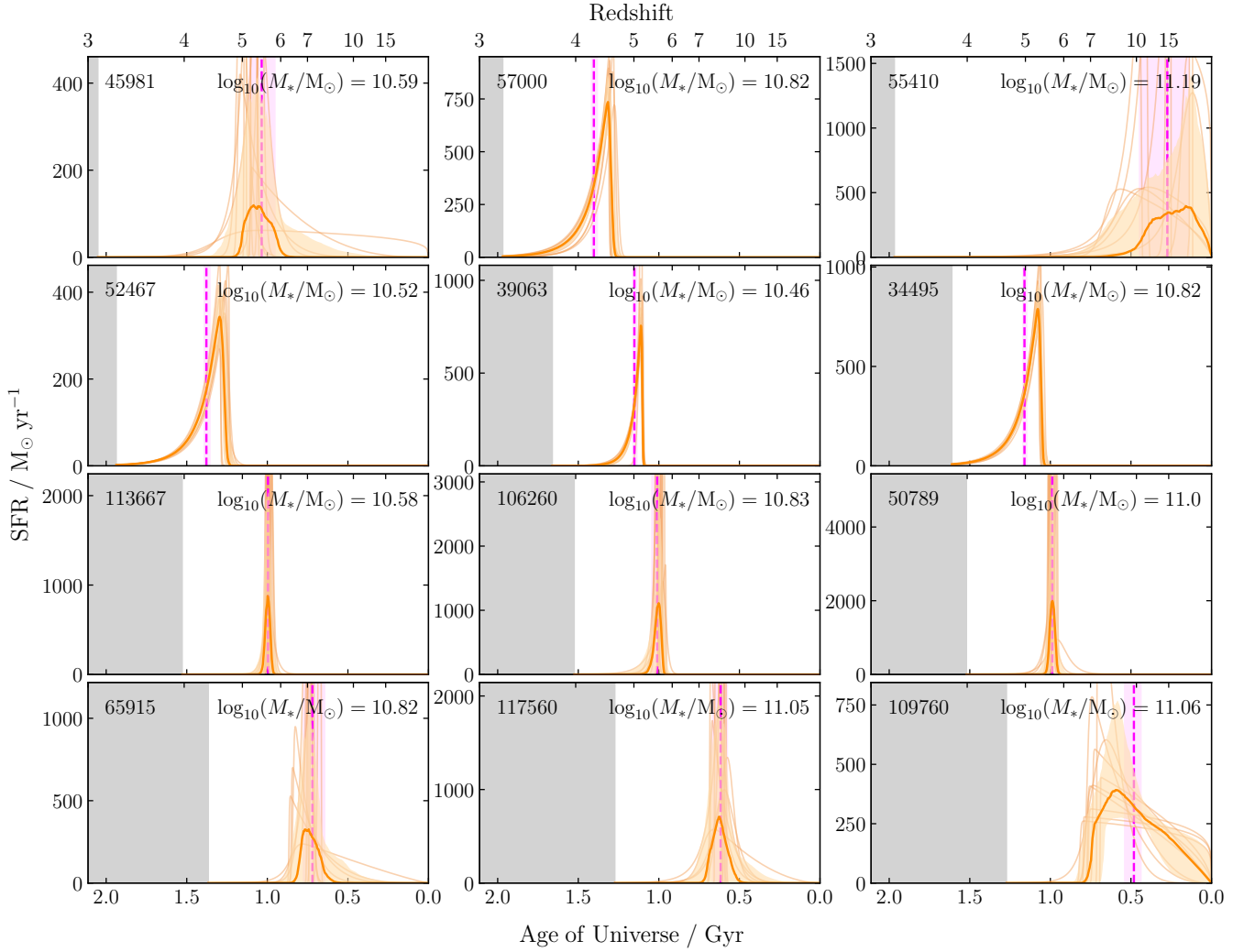


Figure A1. Fitted star-formation histories for 12 of our $3 < z < 5$ massive quiescent galaxies, obtained from BAGPIPES full spectral fitting. The posterior median SFHs (thick orange lines) are plotted alongside their 16th–84th percentile confidence intervals (orange shaded regions). We also show the SFHs of ten random samples drawn from the posterior distributions with lighter orange lines. The vertical pink dashed lines mark the posterior median times of formation (t_{form}), while the pink shaded regions mark their 1σ uncertainties. Cosmic time after each galaxy’s observation is shaded grey.

and $[\alpha/\text{Fe}]$ values to $[\text{Fe}/\text{H}]$, $[\text{Mg}/\text{H}]$ and $[\text{Mg}/\text{Fe}]$, we first convert $\log_{10}(Z_*/Z_\odot)$ to metallicity in mass fraction:

$$\log_{10}(Z_*) = \log_{10}(Z_*/Z_\odot) + \log_{10}(Z_{\odot,\text{A09}}) , \quad (\text{B1})$$

where $Z_{\odot,\text{A09}} = 0.0142$ is the proto-solar metallicity from [Asplund et al. \(2009\)](#). Next, we perform 2D interpolations given the BPASS abundance table to obtain A_{Fe} and A_{Mg} :

$$A_{\text{Fe}} = f_{\text{Fe}}\left(\log_{10}(Z_*), [\alpha/\text{Fe}]\right) \quad (\text{B2})$$

$$A_{\text{Mg}} = f_{\text{Mg}}\left(\log_{10}(Z_*), [\alpha/\text{Fe}]\right) . \quad (\text{B3})$$

This interpolation is performed using the `scipy.LinearNDInterpolator` routine. We then subtract the [Asplund et al. \(2009\)](#) solar

abundance ratios in Table B1 to get

$$[\text{Fe}/\text{H}] = A_{\text{Fe}} - A_{\text{Fe},\odot,\text{A09}} \quad (\text{B4})$$

$$= A_{\text{Fe}} - 7.50 \quad (\text{B5})$$

$$[\text{Mg}/\text{H}] = A_{\text{Mg}} - A_{\text{Mg},\odot,\text{A09}} \quad (\text{B6})$$

$$= A_{\text{Mg}} - 7.60 . \quad (\text{B7})$$

Finally, the Mg to Fe abundance ratio can be directly calculated by

$$[\text{Mg}/\text{Fe}] = [\text{Mg}/\text{H}] - [\text{Fe}/\text{H}] . \quad (\text{B8})$$

B2 The sMILES library

The chemical abundances of sMILES SSPs are labelled in terms of $\log_{10}(Z_*)$ and $[\alpha/\text{Fe}]_{\text{A05}}$, on the [Asplund et al. \(2005\)](#) scale. To perform our conversions, we make use of equation 2 in [Knowles et al. \(2023\)](#), which relates $[\text{Fe}/\text{H}]$, $[\alpha/\text{Fe}]$ and total metallicity:

$$[\text{M}/\text{H}]_{\text{A05}} = [\text{Fe}/\text{H}]_{\text{A05}} + a[\alpha/\text{Fe}]_{\text{A05}} + b[\alpha/\text{Fe}]_{\text{A05}}^2 , \quad (\text{B9})$$

where all abundances are on the [Asplund et al. \(2005\)](#) scale, and the total metallicity assumes the photospheric value $Z_{\odot} = 0.0122$. [Knowles et al. \(2023\)](#) found the coefficients to be $a = 0.66154 \pm 0.00128$ and $b = 0.20465 \pm 0.00218$. Following [Knowles et al. \(2023\)](#), $[\text{M}/\text{H}]$ is defined as

$$[\text{M}/\text{H}] = \log_{10}(Z/X)_{*} - \log_{10}(Z/X)_{\odot} . \quad (\text{B10})$$

This equation can be rearranged to give

$$[\text{M}/\text{H}] = \log_{10} \left(\frac{Z_{*}}{X_{*}} \cdot \frac{X_{\odot}}{Z_{\odot}} \right) . \quad (\text{B11})$$

We make the simplifying assumption that the variation in hydrogen mass fraction is negligible, such that $X_{*} \sim X_{\odot}$, Equation B11 therefore simplifies to

$$[\text{M}/\text{H}] \approx \log_{10}(Z_{*}/Z_{\odot}) . \quad (\text{B12})$$

To use Equation B9, all input values must first be converted to the appropriate [Asplund et al. \(2005\)](#) scale. For sMILES, we perform spectral fitting with $[\alpha/\text{Fe}]$ kept in [Asplund et al. \(2005\)](#) scale, but total metallicity on the [Asplund et al. \(2009\)](#) scale (proto-solar). Therefore, we convert total metallicity to the [Asplund et al. \(2005\)](#) scale by:

$$\log_{10}(Z_{*}/Z_{\odot})_{\text{A05}} = \log_{10}(Z_{*}/Z_{\odot})_{\text{A09}} + \log_{10} \left(\frac{Z_{\odot, \text{A09}}}{Z_{\odot, \text{A05}}} \right) . \quad (\text{B13})$$

Then, we substitute Equation B13 into Equation B9 to calculate $[\text{Fe}/\text{H}]_{\text{A05}}$.

[Knowles et al. \(2023\)](#) note that during the construction of sMILES, empirical $[\text{Mg}/\text{Fe}]$ measurements of MILES stars are taken as a proxy for $[\alpha/\text{Fe}]$. Hence, for the purpose of the conversion, we assume $[\text{Mg}/\text{Fe}] = [\alpha/\text{Fe}]$. It follows that

$$[\text{Mg}/\text{H}]_{\text{A05}} = [\alpha/\text{Fe}]_{\text{A05}} + [\text{Fe}/\text{H}]_{\text{A05}} . \quad (\text{B14})$$

Finally, we convert from the [Asplund et al. \(2005\)](#) scale to the [Asplund et al. \(2009\)](#) scale by

$$[\text{Fe}/\text{H}]_{\text{A09}} = [\text{Fe}/\text{H}]_{\text{A05}} + A_{\text{Fe}, \odot, \text{A05}} - A_{\text{Fe}, \odot, \text{A09}} \quad (\text{B15})$$

$$= [\text{Fe}/\text{H}]_{\text{A05}} + 7.45 - 7.50 \quad (\text{B16})$$

$$[\text{Mg}/\text{H}]_{\text{A09}} = [\text{Mg}/\text{H}]_{\text{A05}} + A_{\text{Mg}, \odot, \text{A05}} - A_{\text{Mg}, \odot, \text{A09}} \quad (\text{B17})$$

$$= [\text{Mg}/\text{H}]_{\text{A05}} + 7.53 - 7.60 . \quad (\text{B18})$$

This paper has been typeset from a $\text{TeX}/\text{L}\text{A}\text{T}\text{E}\text{X}$ file prepared by the author.